



Kent Academic Repository

Mayhew, Ryan (2018) *Using Laboratory Experiments and Hydrocode Modelling to Investigate Hypervelocity Impacts on Spacecraft and Satellites in Low Earth Orbit*. Master of Science by Research (MScRes) thesis, University of Kent,.

Downloaded from

<https://kar.kent.ac.uk/68458/> The University of Kent's Academic Repository KAR

The version of record is available from

This document version

UNSPECIFIED

DOI for this version

Licence for this version

UNSPECIFIED

Additional information

Versions of research works

Versions of Record

If this version is the version of record, it is the same as the published version available on the publisher's web site. Cite as the published version.

Author Accepted Manuscripts

If this document is identified as the Author Accepted Manuscript it is the version after peer review but before type setting, copy editing or publisher branding. Cite as Surname, Initial. (Year) 'Title of article'. To be published in *Title of Journal*, Volume and issue numbers [peer-reviewed accepted version]. Available at: DOI or URL (Accessed: date).

Enquiries

If you have questions about this document contact ResearchSupport@kent.ac.uk. Please include the URL of the record in KAR. If you believe that your, or a third party's rights have been compromised through this document please see our [Take Down policy](https://www.kent.ac.uk/guides/kar-the-kent-academic-repository#policies) (available from <https://www.kent.ac.uk/guides/kar-the-kent-academic-repository#policies>).

**Using Laboratory Experiments
and Hydrocode Modelling to
Investigate Hypervelocity Impacts
on Spacecraft and Satellites in
Low Earth Orbit**

**University of
Kent**

Ryan Mayhew

Supervisor: Dr PJ Wozniakiewicz

**Thesis submitted in consideration for qualification of
'Master of Science'**

Abstract

The near Earth environment has been slowly but surely populated by both natural and man-made debris particles over the past 50 years; this also been dramatically increased due to the deliberate destruction of the Fengun-1C satellite and the accidental collision between the Iridium 33 and Cosmos 2251 satellites. This high number of particles poses a significant risk to any spacecraft travelling through this environment, putting them at danger from hypervelocity impacts – impacts from particles travelling at speeds ranging between 5 and 70kms⁻¹. This thesis has investigated the impacts, and secondary ejecta produced, using a laboratory two-stage light gas gun and also compares the results found with computer simulations of these impacts to investigate whether our modelling systems are effective at predicting damage that may occur. It was found that with an increasing angle of incidence of incoming projectile, the secondary ejecta profiles of projectile and target plates became more defined, with the profile present lower down and closer to the impact site. In regards to the computer modelling, it was seen that a similar secondary ejecta pattern was reproduced; due to computer limitations though, the detail obtained was not sufficient enough to determine whether our current modelling systems are enough to accurately reproduce these impacts or not, and more experimental data & modelling information would be required to fully ascertain whether our understanding and efforts to replicate them are fully developed, giving us the best opportunity to create adequate protection from man-made debris and micrometeoroid hypervelocity impact events.

Acknowledgments

First off, I would like to thank my supervisor, Dr Penny Wozniakiewicz, for all the guidance and support she offered me during my research year, and for the training she provided me with for the Scanning Electron Microscope. I would also like to thank Mike Cole and the School of Physical Sciences; Mike for operating the Light Gas Gun, and the department for the reminder lessons on how Autodyn works from my undergraduate days.

Secondly I'd like to thank my mother and father for always being on the end of the phone whenever I need something, and for giving me a place stay when I needed to clear my head for a couple of days.

Thirdly, I would like to thank Luke Alesbrook and Vassi Spathis for always wanting a cup of tea, being able to provide a napkin when I needed one most, and always being able to lighten the mood in any situation.

Finally, and most importantly, I have to thank my wife, Amber Cunningham. Thank you for always being there and supporting me, for making me realise that however dire the situation seemed, however down I felt and however dark my days became, you were always able to lift my spirits, make me smile and give me the kick I needed to keep on going.

Contents

Abstract	1
Acknowledgments	2
Contents	3
Chapter One: Introduction	5
1.1 Dust in the near Earth environment	5
1.2 Studying Cosmic Dust and Space Debris in the near Earth environment	7
1.3 Methods of investigating the impact process during Low Earth Orbit impact events	10
1.4 The Project Aim	11
Chapter Two: Equipment, Software and Methodology	13
2.1 The University of Kent's Two-Stage Light Gas Gun	13
2.1.1 Using the Light Gas Gun	15
2.2 ANSYS Autodyn Hydrocode Modelling Software	21
2.2.1 Impact Event Hydrocode Simulations	24
Chapter Three: Results from the Two-Stage Light Gas Gun	28
3.1 Aluminium Targets	31
3.1.1 30 Degrees – G240316/3	31
3.1.2 45 Degrees – G240316/1	40
3.1.3 60 Degrees – G240316/2	49
3.2 Soda Lime Glass Targets	56
3.2.1 30 Degrees – G250216/1	57
3.2.2 45 Degrees – G110216/1	62
3.2.3 60 Degrees – G110316/2	68
Chapter Four: Results from the Hydrocode Modelling Simulations	73
4.1 Aluminium Targets	73
4.1.1 30 Degrees	73

4.1.2 45 Degrees	75
4.1.3 60 Degrees	76
4.2 Soda Lime Glass Targets	76
4.2.1 45 Degrees	77
Chapter Five: Conclusions	79
References	81
Journals and Proceedings	81
Websites	84

Chapter One: Introduction

This beginning chapter will provide an introduction to this thesis. It will present background information on the near Earth environment, space debris and cosmic dust, the impact events that occur due to these particles, as well as the investigatory processes for analysing spacecraft and satellites subsequent to these events. It will end with the aim of the project for this thesis, outlining the research to be undertaken.

1.1 Dust in the near Earth environment

Over the past half a century, the near Earth environment of space has changed dramatically, from a very desolate environment with the occasional meteoroid passing through it, to one that is now populated by thousands of artificial satellites dedicated to communications, navigation and the collection of data. The environment of space, with extreme temperatures and temperature variations, oxidising effects of atomic oxygen (Waters et al., 2007) and direct exposure to solar radiation (UV and cosmic rays) (Grossman and Gouzman, 2003), take their toll on objects residing there: over time, these satellites begin to weather, creating a population of extremely small particles orbiting the planet. This space debris can occur in varying sizes, shapes and compositions depending on its origin: from paint flakes derived from the protective coatings applied to satellite components to small chunks of solder that have detached from electronics. Satellites in low Earth orbit (LEO) travel at speeds ranging between 6.9 kms^{-1} and 7.8 kms^{-1} depending on their altitude (LEO altitude is defined as two hundred to two thousand kilometres, and velocities differ to keep orbits stable at varying altitudes [Bradley and Wein, 2009]). However the relative velocities of differing satellites can be very large, theoretically reaching around 15.6 kms^{-1} , assuming both satellites were travelling with velocities of 7.8 kms^{-1} towards a head-on collision. Consequently each piece of space debris poses an impact hazard to other satellites. Despite their small size, space debris can create extensive damage upon, and after, impact. Tiny cosmic dust particles, which are mainly thought to originate from asteroids and comets, can

also collide with, and damage these satellites with velocities ranging between 5 and 70kms⁻¹ (Graham et al., 2001). Impacts by both these naturally occurring micrometeoroids and the man-made space debris result in the generation and ejection of additional debris which can go on to damage other spacecraft. One can imagine that, as the near Earth environment becomes more saturated with space debris, the likelihood of an impact occurring increases and furthermore, as more impacts take place, new debris is produced, resulting with higher chances for further impacts (The Kessler Syndrome – Kessler and Cour-Palais, 1978).

One such event of man-made debris, which could also have a profound impact on the theory of The Kessler Syndrome, was the intentional destruction of the Chinese meteorological satellite, the Fengyun-1C. As discussed by Johnson et al. in 2008, the destruction of the satellite due to a hypervelocity impact with a specially designed ballistic object “created the most severe artificial debris cloud in Earth orbit since the beginning of space exploration”. It is believed that this hypervelocity impact created more the 2000 new individual debris pieces of size 10cm or bigger; this was an almost sudden one-third increase in the number of debris present in LEO, which had taken approximately 50 years to reach this level. It is predicted that some of the larger debris fragments will remain in LEO for a minimum of 100 years; this would, very clearly, pose a massive problem in regards to the future of LEO-based missions.

Another event which will have dramatic and long-lasting effects on the near Earth environment was the collision of the American Iridium 33 and the Russian Cosmos 2251 satellites (Wang 2010). This collision occurred in early February 2009, marking the first in-orbit collision between two satellites. Catalogued by the U.S. space tracking system, this collision released 1632 debris fragments into orbit around the Earth, only further increasing the possibility of consequential impacts on other satellites and posing an even greater danger to anything passing through this region of space.

1.2 Studying Cosmic Dust and Space Debris in the near Earth environment

Determining the source of an impactor is important as not only can the different compositions of possible impactors affect the damage done to a spacecraft in an impact event, but the data can provide valuable insights into the abundances, and hence, a level of hazard each population (natural vs. man-made) can pose. Furthermore, it allows us to build up an idea of the populations of particles in different regions of space – knowledge that is extremely important when designing a spacecraft, since this will influence the choice of materials used in, and the amount of, protective shielding built for the spacecraft. For example, LEO is likely to be populated by a large amount of man-made debris, as it is used as a primary location for the majority of man-made satellites (just under 55% of all satellites currently in orbit (Union of Concerned Scientists, 2017)). In contrast, a spacecraft moving in a direction out of the Solar System, on a path through the asteroid belt, will come into contact with a higher percentage of natural micrometeoroids. This is vitally important to be aware of as impacts involving cosmic dust from an asteroid or comet occur at velocities between 5kms^{-1} and 70kms^{-1} (Graham et al., 2001). In comparison, impacts involving space debris typically occur at velocities below 5kms^{-1} . Even though micrometeoroids are very small in size, they still pose considerable a threat to spacecraft. The damage sustained from these impacts over a long period of time can create weathering of the spacecraft's surface, much like the surface of the Moon, weakening its structure and leaving it in a much more vulnerable state to further damage from subsequent hypervelocity impacts.

Based on astronomical observations, it has been estimated that over 500,000 particles larger than 1cm reside in LEO (NASA n.d.). The populations of particles smaller than 1cm in LEO are not well established, as they are harder to observe and track. Estimates therefore have to be obtained by analysing the impacts that occur on spacecraft. These have been studied by various authors, with emphasis on determining the relative abundances of naturally occurring micrometeoroids and man-made space debris; there have been many opportunities to examine space-exposed surfaces and hardware, such as the

Long Duration Exposure Facility (LDEF) (e.g. See et al., 1990), The Hubble Space Telescope (HST) (e.g. Kearsley et al., 2005), Space Shuttle Orbiters (e.g. Bernhard et al., 2001), The Solar Max Satellite (e.g. Warren et al., 1989), the MIR Space Station (e.g. Hörz et al., 2000) and the International Space Station (e.g. Carpenter et al., 2005).

To determine the size and composition of the debris, and then use this information to identify a possible origin, varying methods of analysis are employed on the impacted surface. Scanning electron microscopy with energy dispersive X-ray spectroscopy (SEM-EDX) can be used to obtain images that reveal the topography of the impact site together with qualitative chemical data for any residue present within the impact crater that was produced. Studies of impact craters on spacecraft surfaces have shown that residues within them preserve details of the composition of the impacting debris and can be used to infer an origin for the impacting particle such as micrometeoroids, solid rocket motor fuel, paint, etc. (Bernhard et al., 1997). For example, if the EDX data shows that Chromium, Nickel and Iron are present within a crater residue, then the impactor is likely to have been composed of stainless steel (Christiansen et al., 2004). Such compositional data, combined with the details of the impact crater morphology (shape, diameter and depth) can then allow the details of the debris size and speed prior to the impact to be estimated (Bernhard et al., 2001; Christiansen et al., 2004). If multiple impact sites of similar topographical profiles with similar crater residue are present on an analysed surface, and the location of the satellite/spacecraft when impacted is known – e.g. LEO, Geosynchronous Orbit, or Areocentric Orbit – a picture of the distribution of different types, sizes and compositions of debris can be built; EVOLVE – a one-dimensional model which was able to describe the LEO debris environment – (Johnson et al., 2001), and LEGEND – an LEO-to-GEO Environment Debris model, is a three-dimensional model describing orbital debris information as functions of time, altitude, longitude and latitude – (Liou et al., 2004) are two examples of what can be done with gathered intelligence on hypervelocity impacts.

Further methods of impact crater analysis include using an epoxy or dental mold to gain an impression of the impact crater. This method was developed where the analysis of an impacted site is time-limited, requiring a good way to record or collect the physical evidence without keeping the actual impacted surface. For example, if the vehicle being analysed is a shuttle orbiter, and it needs to be returned for its post-mission service, but the sampling of impact craters may interfere with this (Bernhard et al., 2001). An SEM can then be used on the impressions for topographical information, and if the impression mould has picked up some impact residue, then it is also possible to use EDX to gain compositional data of the debris. This method works by using the impression in the same way you would the impact site itself; using a scanning electron microscope to gain a better understanding of the morphology of the impact crater (only with an impression mould, in reverse), and the EDX to obtain qualitative chemical data for any residue – as the chemical composition on the mould used for the impression is known, residue chemical data can be easily identified. Adhesive tape or a soft wooden probe can also be applied to the impact site to gather impact particles, however, the size of the impactor cannot be inferred as no physical dimensions are being analysed (Bernhard et al., 2001).

To conclude, the task of obtaining information regarding the chemical and crystallographic make-up of impact sites is not the easiest to achieve due to the different factors mentioned, but it can still be done. Using SEM/EDX can work, but it does have its drawbacks. One being that with larger craters, a shadow-like effect can occur. This can in turn obscure the central pit and walls of the crater (Wozniakiewicz et al., 2009) meaning that chemical information of the area covered cannot be obtained. Another drawback would be the difficulty of using SEM/EDX techniques on in-situ impact sites; these could be on the body of a returned space shuttle, the protective shielding on the ISS, or even on one of the investigative surfaces of the LDEF. To overcome this, a Focused Ion Beam (FIB) and Transmission Electron Microscopy (TEM) can be utilised (Wirth 2009). FIB works by using a beam of focused ions, usually Gallium (Heaney et al., 2001), to either ablate the surroundings of the impact site to gain better access to it for analysis, or to cut away an extremely thin section of the sample

which can be analysed using TEM (Giannuzzi et al., 1997). But with most things, FIB does have a negative side effect – when using the focused gallium beam, gallium ions may sometimes be deposited on the surface of the sample, which may then interfere with or alter the sample being analysed (Graham et al., 2004). When using TEM, an extremely thin sample is needed, described as electron transparent, where electrons are transmitted through the sample area to gain an image based on the interactions between the electrons and the sample. There are other tools which can help in preparing a sample for analysis such as ‘microtweezers’ and ‘microneedles’ (Westphal et al., 2002); microneedles are used to dig very small trenches or tunnels to gain access to more imbedded particles and grains, and the microtweezers are for the extraction of these grains if and when needed. With these preparation techniques and the FIB & TEM analyses type used in conjunction with SEM/EDX, a better picture of the quantitative chemical crystallographic make-up of particles and impacts can be obtained than using just the SEM/EDX technique alone.

1.3 Methods of investigating the impact process during Low Earth Orbit impact events

Not only is it important to know the possible impactors, sizes, compositions and velocities that a spacecraft may face in the near Earth environment, it is also vital to understand how different materials respond and react to hypervelocity impacts. We must determine which materials are best to be used in space, and which are not; materials which disintegrate upon impact could cause a significant problem to a satellite, or even possibly loss of life to a manned spacecraft mission. With this in mind, it is imperative that we investigate any and all impact sites observed so as to gain as much information and data possible to create a more complete picture of the possible dangers these impactors can pose, One way this can be done by experimenting in the laboratory, creating hypervelocity impacts at well constrained velocities with known materials, of particular sizes and shapes to observe what happens when all of these variables are known. This data can then be compared to current findings from real hypervelocity impacts such as those found on the Solar Max

Satellite or LDEF, potentially providing insight into how fast it was travelling, or what it was made up from and its possible origin.

Another way of investigating hypervelocity impacts is by using computer simulations, such as hydrocode modelling simulations. Hydrocode models simulate fluid flows at all speeds by taking a 3-dimensional model, breaking it down into a mesh of cells and calculating the forces, both external and internal, acting upon each cell of the entire system over small time steps (Collins, 2002). At the end of each time step, the model geometry is adjusted based upon the calculated results and the calculations begin again, with the calculations finishing when a wrap-up criteria has been reached; examples of this being that the time limit imposed on the model has been achieved, the cycle limit for the model has been reached, or other user-created wrap-up limits have been met.

1.4 The Project Aim

The aim of this project is to investigate the generation of secondary ejecta produced by impacts in LEO through laboratory experimentation using a light gas gun and complementary computer simulations. The focus will be on Zirconium projectiles fired into targets of Aluminium alloy plates and Soda Lime Glass blocks. Aluminium alloys are commonly used within spacecraft structures (as well as external shielding such as protective covers for viewports) due to having a high strength-to-weight ratio; aluminium on its own would be much too soft to be used, so using an alloyed version gives it much greater strength without adding too much weight. They are also extremely easy to create, cast and machine giving them an edge over other materials when selecting what would be most appropriate to use. When the spacecraft is to be a manned mission, windows, or viewports, are sometimes inbuilt into the structure. These viewports are commonly composed of fused silica or quartz glass, but in a few rare instances, but have also been created from diamond and sapphire. The craters formed and secondary ejecta produced will then be analysed using image processing software and SEM-EDX. The findings will then be compared with hydrocode modelling simulations of these events to evaluate our current understanding and ability to replicate hypervelocity impacts. Many studies have been completed focusing on the analysis of spacecraft surfaces post-impact

event once returned to the Earth's surface, the Hubble Space Telescope (Graham et al., 1999) and the LDEF (Zolensky et al., 1995) being two examples. Studies involving numerical modelling have also been completed, such as those by Collins et al. in 2004 and Davidson et al. in 2011, but there been few studies directly comparing a hypervelocity impact event to a hydrocode simulation of the same event as the conditions of the impact, such as impactor velocity, size and composition, are very difficult to determine post-impact. This thesis will try to bridge this gap between simulation and real-life hypervelocity impact events, and to try and provide a direct comparison between the two, to determine whether our current understanding of these events is sufficient, and to possibly find new ways of classifying the impactor's velocity or impacting angle based upon the secondary eject produced in the impact.

Chapter Two: Equipment, Software and Methodology

The following chapter will introduce the physical experimental equipment and computational software used in the undertaking of the research for this thesis, as well as outlining the methods used during the experimental work. It will also include both information on the make-up of the physical targets used within the light gas gun and the computer simulation model set-ups.

2.1 The University of Kent's Two-Stage Light Gas Gun

The University of Kent's School of Physical Sciences department have an operational Two-Stage Light Gas Gun (Burchell et al., 1999). Figure 1 has been labelled showing the main components of the light gas gun, with Figure 2 displaying the inside of the target chamber, and Figure 3, a schematic diagram of the inner workings of the light gas gun.



Figure 1 - Labelled images of the Light Gas Gun showing its major components: (1) Powder Chamber, (2) Pump Tube, (3) Launch Tube, (4) Blast Tank, (5) Dual Laser Blanket connected to oscilloscope, (6) Target Chamber.



Figure 2 - Image showing the inside of the Target Chamber: (1) The connecting tube between the Blast Tank and the Target Chamber through which the projectile travels, (2) Target Mounting Bracket attached to the Target Chamber door where the user-defined target can be fitted.

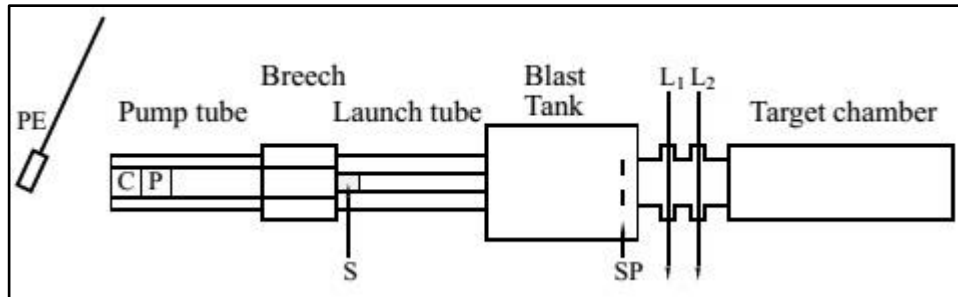


Figure 3 - A Schematic Drawing of the Light Gas Gun showing the inner workings: (PE) pendulum, (C) Cartridge, (P) Piston, (S) sabot, (SP) Stop Plate, (L₁ & L₂) Dual Laser Blanket [Burchell et al. 1999].

The two-stage light gas gun works by providing acceleration to the piston by the burning of gunpowder within the cartridge. The piston compresses a low relative molecular mass gas, creating a pressure difference, rupturing a burst disc and accelerating the projectile contained within the sabot. Table 1 below shows the relation between desired velocity and gas conditions needed for the operation of the gas gun. The sabot itself can either be a solid block of nylon, or it can be a 'split' sabot; this is where the sabot has been cut into either two or four pieces (a split sabot cut into four pieces has been used in the following experiments). When the split sabot travels through the blast tank, it spins due to the rifling of the launch tube. The pieces of sabot then begin to move off of the main gun axis, whilst the projectile that was contained within it, continues to travel on the main gun axis. The sabot is then caught by the stop plate, and the projectile

travels through a small hole in the centre directly through the dual laser blanket. The lasers are connected to a digital oscilloscope; as the projectile moves through them creating a disturbance in their displayed signals, the velocity of the projectile can be calculated (as their separation distance is known) with an error better than $\pm 1\%$ (Burchell et al., 1999). The projectile then moves into the target chamber and impacts into the user-designed target.

Desired Velocity (kms⁻¹)	Gas to be used	Gas and Gunpowder Condition
1.1	Nitrogen and SF ₆	14 bar SF ₆ raised to 40 bar with Nitrogen and 10g of gunpowder
1.2-2.2	Nitrogen	40-70 bar and 8-10g of gunpowder
3.3-4.3	Helium	45-70 bar and 10g of gunpowder
4.4-5.7	Hydrogen	35-70 bar and 8-10g of gunpowder

Table 1 - Table showing the attainable velocities with the Light Gas Gun and their Gas/Gunpowder dependencies [Burchell et al., 1999].

2.1.1 Using the Light Gas Gun

Before beginning the main experimental firing shots were started for this research, two test firings were undertaken. These two shots all consisted of the same target plate – a 3mm thick, square sheet of aluminium –but had different projectiles fired towards them; the first was a stainless steel sphere, the second a soda lime glass sphere. Both projectiles were fired directly at the aluminium plates. These test shots were completed so that there was some understanding of what a hypervelocity impact site could look like, and also to see the physical difference, if any, in the shape and the size of the craters that the impacts generated. Also, after the main shots were finished, a third test shot with the same conditions as the first two was then completed, this time using a zirconia sphere projectile. This was to be aware of any differences between impacts due to projectile, and to also see what a front-on impact would look like with the

projectile type used in the main experiments. The following figure shows the set-up of the test shots.

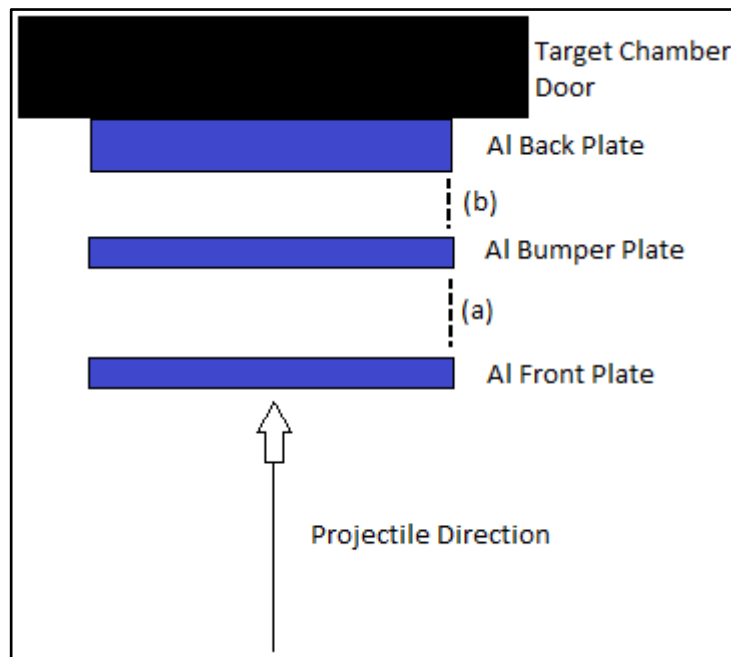


Figure 4 - Schematic showing a top down view of the target set up for the three test shots. The projectile direction, shown by the arrow, was directly aimed at the Aluminium plates, with the plates in blue (the first two being 3mm thick, and the back plate being 5mm thick) and the Target Chamber Door in black. The gaps between the Aluminium plates were 80mm (a) and 37mm (b) [not to scale].

After the first two test firings were completed, the main experimental shots took place; the first being a zirconia projectile contained within a split sabot (chosen to be used for all experimental shots as the zirconia, aluminium, copper and soda lime glass can all be easily distinguished between upon elemental analysis) fired at an aluminium plate at an angle of 45° , with a copper 'witness plate' fixed in place at the end of, and perpendicular to, the aluminium plate to capture the secondary ejecta from the impact. Behind the front aluminium plate was a second aluminium plate (the 'bumper plate') to capture any 'burst-through' ejecta, simulating internal damage (if any occurred), which could then also be analysed. After this shot, the aluminium bumper plate was exchanged for a copper bumper plate, so as to differentiate between any burst-through aluminium (from the front plate) and aluminium from the bumper plate upon the analysis stages. The shot for 45° was then repeated with the new bumper plate

set up, and two further shots were undertaken where the impact angle was changed to 30° and 60° for each shot. The set up was the altered again; the aluminium front plate and copper bumper plate were removed and a soda lime glass block was inserted for the projectile to be fired at, with a copper witness plate still used to capture secondary ejecta, again fixed perpendicular fashion and the end of the soda lime glass block. The following figure shows the main experimental shot/target set up.

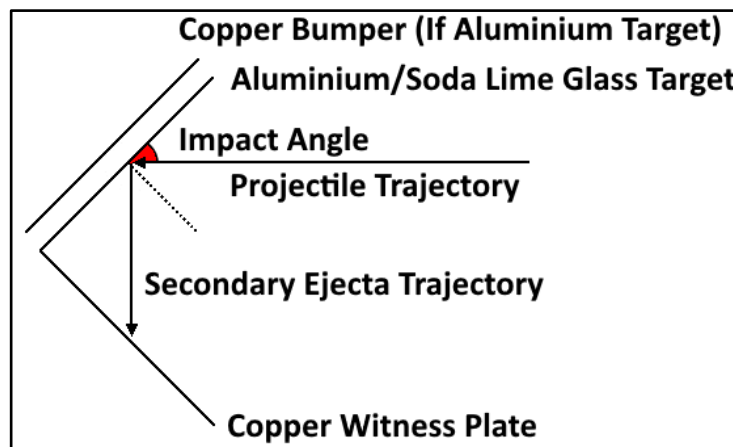


Figure 5 - Top down schematic for the main experimental shots showing the trajectories of both the projectile and secondary ejecta, the placement of the Aluminium/Soda Lime Glass Targets (and Copper Bumper Plate for the Aluminium shots), the Copper Witness Plate, and the Projectile's impacting angle upon the target.

As the target plates were different, an altered physical target set-up was used for the separate target types, but was maintained within the two target conditions. Measurements were made to ensure the shots within the conditions had the same physical set ups, where the tables below present the dimensional information for these conditions.

Aluminium (Al) Target Component	Measurement (mm)
Al Front Plate	3
2x Small Spacer	14 (7mm each)
Copper Bumper Plate	1
2x Small Spacer	14 (7mm each)
1x X-Large Spacer	50
1x Large Spacer	37
Al Back Plate	3
1x Bracket Nut	11
Target Bracket Mount Base	N/A

Table 2 - Table outlining the physical measured set up for the Aluminium target experimental shots, starting with the target plate and ending with the target mount, with all measurements given in millimetres. All spacers used (along with the Al back plate) were the same ones used between all Aluminium target shots (even though still being measured between each shot when target mounting was dismantled to ensure consistency).

Soda Lime Glass Target Component	Measurement (mm)
Soda Lime Glass Block	18
Al Plate with rubber insulate¹	5
1x XX-Small Spacer	2
1x X-Small Spacer	4
Al Middle Plate	3
1x X-Large Spacer	50
1x Larger Spacer	37
Al Back Plate	3
1x Medium Spacer	17
1x Bracket Nut	11
Target Bracket Mount Base	N/A

Table 3 - Table outlining the physical measured set up for the Soda Lime Glass target experimental shots, starting with the Soda Lime Glass Block and ending with the target mount, with all measurements given in millimetres. All spacers used (along with the Al middle & back plates) were the same ones used between all Soda Lime Glass target shots (even though still being measured between each shot when target mounting was dismantled to ensure consistency).

The following image was taken after completing the target set-up for one of the soda lime glass experimental shots, illustrating how the set up was achieved, with all main components included for the target mounting.

¹ Note regarding the usage of the Aluminium plate with rubber insulate – there was a concern that when the hypervelocity impact occurred, that the force of the impact could break the glass more than anticipated. The decision was made to use the aluminium/rubber insulation plate, as it may have helped to keep the soda lime glass block more intact post-impact and maximise the chances of retrieval.

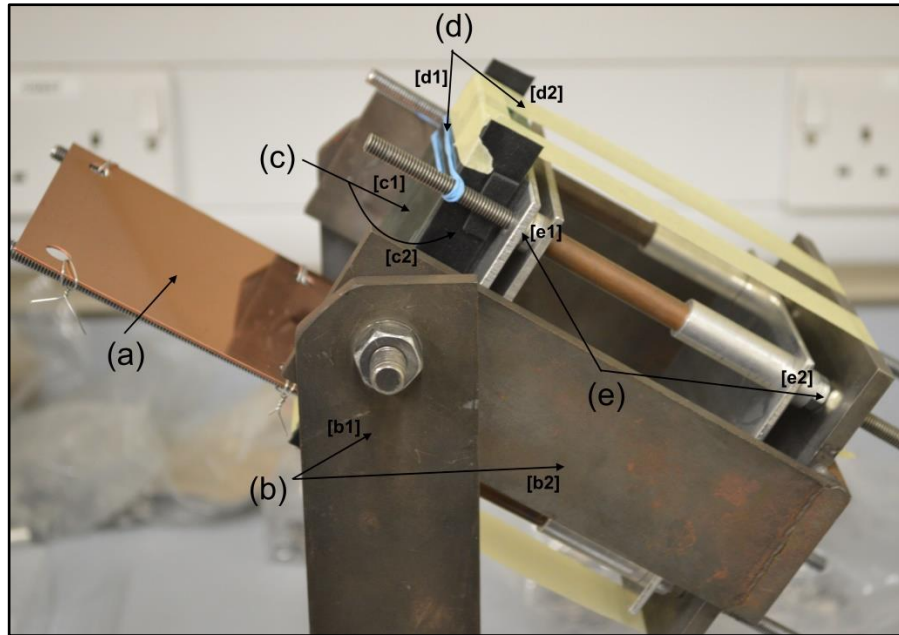


Figure 6 – Image showing the target set-up (from a bottom up perspective) of a soda lime glass experimental target. The marker (a) shows the Copper witness plate and (b) showing the target bracket mount; the [b1] portion is static and the [b2] portion is able to swivel, gaining the required angle for each shot. The soda lime glass target itself is shown by (c), where [c1] is the actual target block and [c2] shows the rubber mounting strips, which helped to keep the block stable and stopped upwards/downwards movement. Marker (d) illustrates more stabilisation aids, [d1] being an elastic band and [d2] some mounting tape which helped to stop any motion in projectile trajectory plane. The final marker (e) shows the rest of the target components starting with the Al plate with rubber insulate at [e1] and ending with the bracket nut at [e2].

As stated, Figure 6 shows the set-up of a soda lime glass target; the aluminium targets needed less stabilisation and mounting aids as the aluminium plates were easier to mount onto the target bracket. Using the information from Tables 2 & 3 and the image of Figure 6, the physical set-up of the aluminium targets can be inferred.

After each shot was completed, it was carefully disassembled (extremely so in the cases of the soda lime glass targets due to the fragility of the glass blocks post experimental firing) from the target bracket mounting, sectioned up and labelled for analysis. The next shot could then be readied for by setting the angle of the target bracket mount – 30°, 45° or 60°, whichever angle shot was to be undertaken next – and preparing the components for the desired targets (outlined in Tables 2 & 3), whether that be for the aluminium targets or the soda lime glass targets.

All experimental tests were aimed to have the projectile fired at the targets with a velocity of around 5kms^{-1} – this was due to two main factors; one being that this was an easily achievable velocity using the two-stage light gas gun, and the second being due to previously calculated micrometeoroid velocities, and also possible varying speeds of satellites in orbit around the Earth. As previously stated, cosmic dust from asteroids and comets can potentially have velocities ranging between 5kms^{-1} and 70kms^{-1} (Graham et al., 2001), and satellites can travel at speeds between 6.9kms^{-1} and 7.8kms^{-1} in Low Earth Orbit – with this information taken into account, coupled with the aim of this thesis, which was to investigate micrometeoroid impacts onto satellites and other spacecraft in Low Earth Orbit, the projectile velocity was decided to be, or as close to as experimentally possible, 5kms^{-1} .

2.2 ANSYS Autodyn Hydrocode Modelling Software

Autodyn is a computerised hydrocode modelling software system utilised by a variety of companies, departments and even governmental authorities to simulate what could happen in a diverse array of situations, so as to give a better understanding of the outcome of those situations. One such usage could be by a military organisation to attempt to replicate what may happen if an armoured tank or a transport vehicle was attacked by differing types of weapon fire out in the field, and what affect this may have on the vehicles, or the people, within them. It can also be used by car manufacturers to investigate what kind of stresses a car may go through when it is being used during the time that the car is being designed, so as not to overlook anything in further design & construction phases. Space authorities, such as NASA or ESA, could also utilise this software for similar uses; hydrocode modelling in this instance can be used as both, a kind of ‘what if’ tool before an event happens, and also as a retrospective investigational tool after something has happened. Both of these two uses are very important as it is not as easy or as cheap to test or to physically trial a lot of incidents that could occur in space, such as, the damage sustained to a new satellite by small pieces of an old, broken apart satellite still in orbit. Using hydrocode modelling as a ‘what-if’ tool would help to ensure that when physical testing cannot be undertaken, then the design, manufacture and

production phases of space-faring technology would still be able to take into account as much data and results of a computer-simulated fabricated event as possible. It bases the ideas used in the design and creation of the item on scientific analysis of possible outcomes from different events that could happen to the item in question. It would also aim to, from the retrospective viewpoint, provide more in depth information on what exactly happened during a recorded incident in space, or even during launch or re-entry into the Earth's atmosphere. This data can then be used in another designing, manufacturing, and production cycle to help with the next iteration of the technology being created. This could mean updating its protection systems to sustain less possible damage from outside influences, ensuring that it can still perform its main purpose if it does become damaged, and to make sure that the new iteration's design and manufacture will incorporate all applicable information, results and findings that are relevant to its creation, its function and its overall mission longevity.

Autodyn allows the user to have complete control over the viewing, the set-up, and the overall creation of their simulation by giving them multiple modules within the software to manipulate their desired computer-generated environment. The in-house control panel can be seen below.

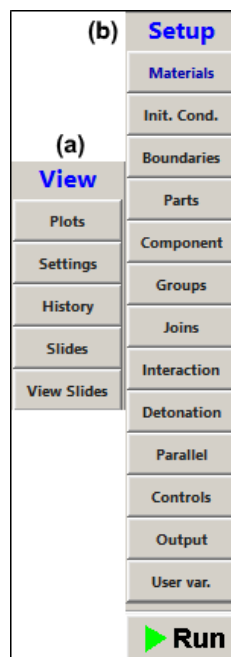


Figure 7 - Image showing the Autodyn User Control Panel (The 'View' section, (a), is displayed above the 'Setup' section, (b), within the Autodyn software package).

The 'View' control pane – (a) within Figure 7 – allows the user to customise how they see their simulation; things such as the velocity vectors can be viewed on the model as arrows, a grid can be displayed to show the physical location in 3D space of where parts of the simulation are in respect to the origin location, and whether gauges (points that are defined by the user within the simulation used to measure a variety of user-chosen variables – velocity, pressure, temperature, etc.) are seen during the computer simulation. The View pane also gives the user the ability to create, view and interact with images (or 'slides') from the emulation, create their own moving images of parts of the interactions, and view 'history plots' – graphs which again can show varying information, such as energy, momentum, and the information from the user-created gauges.

The 'Setup' pane – (b) within Figure 7 – gives the user the tools to be able to create their chosen environment within the system via the different modules contained within it. For example, the 'Materials' module is where the user selects what materials (e.g. Aluminium, Gold, Copper, Water, etc.) will be used within the system, and can give the option of creating a 'new' material that is not contained within the Autodyn Material Library. The 'Init. Cond.' module (Initial Conditions) is where velocity can be defined; this module also gives the ability to create angular velocity and radial velocity, and the option of bonding this velocity to certain previously chosen material. Within the 'Parts' module is where the environment's pieces can be created – such as bullet, a firing mechanism, and a gun if simulating a rifle – using a variety of system 'solvers' (a 'solver' is the way the system will solve the simulation, using the mathematics linked with each type of solver, during the system's run). It guides the creation of each part, allowing the selection of its origin location, its size, the number of nodes it is to be created with, and also the material it is to be made up from, or to be 'filled' by. The 'Interaction' module gives control over what happens when two or more pieces come in to contact (interact) with each other within the model – it must be noted that this module has two types of interaction options available for use; the first is 'Lagrange/Lagrange' Interactions, which is to be used when interactions are between parts that are all Lagrangian type parts. The second is 'Euler/Lagrange' Interactions, which is to be used when interacting parts will be both Lagrangian and Eulerian type parts. The 'Controls'

module gives the user the command over the solver controls for the model. The main criterion to input for the simulation is the 'Wrapup Criteria'; these are the options which will stop, or force the system to stop the simulation. The maximum number of cycles and time limit can be set by the user, which will force the system to end the run if either of these limits is reached. The 'Energy Fraction' can also be set (as a decimal which will be converted to a percentage), which will also end the simulation if the energy error exceeds this value percentage. The 'Energy Reference Cycle' is the cycle number the user wishes Autodyn to begin checking for the energy error. Furthermore, this module gives other control options, such as 'Timestep', 'Damping' and 'Solver' options, command over Gravity if the user wishes this to be included in their model, and 'Erosion' control – when or how the system will remove elements or nodes from the model during the run.

One of the most important modules is the 'Output' module. This is where the user decides when, how often and what variables are saved, or outputted, from the system based on either cycle number or a time limit, at what frequency the history tables are written, and also whether an image is captured and outputted of the simulation, and at what point this happens.

At the bottom of the 'Setup' pane is one final button – the 'Run' button. When this is pressed, the system will begin running the simulation by taking into account all user-defined options and criteria, ending the created model only when the Wrapup Criteria have been met, or when the Autodyn system encounters an error during the simulation and cannot continue with running the model.

2.2.1 Impact Event Hydrocode Simulations

For the hydrocode model simulations, two main simulations were created at first – one for the aluminium target set up, and the other for the soda lime glass set up. These simulations were then altered so that the different angles of 30°, 45° & 60° would be taken into account.

The set up would have to be as close to the real-life laboratory experiment as possible, so both target-type set-ups were created with a projectile of 1.5mm diameter, as this is what the real-life impactor's size was. In both conditions, the impactor was filled with pre-loaded material of Zirconium (the material models of the materials used can be seen in the figure below). The FLOATGLASS material seen in Table 4 was used as a substitute for the soda lime glass – this was because Autodyn did not have a soda lime glass material loaded within its library, and the correct material properties for the soda lime glass used could not be found to create it within the software.

Loaded Material	Equation of State	Strength Model	Failure Model
Aluminium	Tillotson	None	None
FLOATGLASS	Polynomial	Johnson-Holmquist	Johnson-Holmquist
Zirconium	Shock	None	None

Table 4 - Table showing the material models of the three materials used in the hydrocode models. The three materials used, along with the material models presented here, were all loaded from Autodyn's in-built material library.

The next step was to create the 'Initial Conditions' for the impactor. As the velocity was known based on the angle it impacted the target plates with, trigonometry was used to calculate the speeds needed for the x and z components to ensure the projectile impacted at the correct angle. The below figure displays these velocities input for each condition.

Target Set-Up	Known Velocity [km/s]	x-Component Velocity [km/s]	z-Component Velocity [km/s]
Aluminium 30°	4.79	2.395	-4.148
Aluminium 30°	5.25	3.172	-3.712
Aluminium 30°	4.85	4.000	-2.425
Soda Lime Glass 30°	4.96	2.840	-4.300
Soda Lime Glass 30°	4.57	3.230	-3.230
Soda Lime Glass 30°	4.88	4.230	-2.440

Table 5 - Table showing the Known Velocities to replicate, taken from the laboratory experimental shots and the calculated the velocities needed in the x-directions and the z-directions for the Initial Condition within Autodyn [NOTE – all z-component velocities are negative as this was the direction that the particle was to travel in Autodyn].

Once the initial conditions were created within the system, the two target plates needed to be created – to cut down on complexity level, the plates (and particle) were created in such a way they were cut down the centre, with the ability in Autodyn to then mirror the simulation in of the axis planes; instead of having the whole aluminium plate built with dimensions of 100x100x3mm (LxHxD – L being length, H being height and D being depth), it was created with dimensions 100x50x3mm. The same was also done for the glass block; instead of being built with dimensions 114x62x18mm, it was built with dimensions of 114x31x18mm. The impactor was built in the same fashion; instead of a sphere of diameter 1.5mm, a hemisphere with diameter 1.5mm was created. The flat surface of the hemisphere was aligned with the program so that it was at the same level as the base height of the target plate – this meant that when the model was mirrored in the y-plane, the hemisphere would become a whole sphere, and the half-target plates would become full sized. When building the parts, they were created using the SPH part type, and then each piece of the model required was ‘filled’ with SPH nodes with the corresponding material for the piece it was filling. The SPH solver was used as it was hoped that, as it creates each part of the model out of very small nodes, the increased number of moveable nodes would be able to replicate the laboratory experiments better than having a solid block of material. Once the parts were filled with both the materials and initial conditions needed, the interaction gap size was automatically calculated by Autodyn, and the user controls were entered manually. The cycle limit for all simulations was set to 100,000 cycles and the time limits were set at 100. The energy fraction was set at 0.05, but the cycle to check the energy fraction was set over the maximum cycle, meaning the system would never check the energy fraction. The save cycle was set to start saving information from the simulations on the first cycle, and would then save every 2500 cycles, ending once the simulation had finished. It must be noted here that an EXEDIT file was used during the simulations. The user created subroutine was inputted into the simulations with the express purpose of imitating the copper witness. It did this by creating an invisible plane (chosen to sit in the simulation at the same coordinates as the witness plate would have in the experimental) and slowing down any particle moving through it by such a high factor, that when the simulation had wrapped up, the particles caught by this

plane had hardly moved. This meant that a witness plate was not needed to be built into the simulations, again increasing the complexity. This EXEDIT file was set to be activated, or 'called', on every cycle the simulation ran so as to ensure no particle hitting this plane was lost when it came to look at the results.

Once all of this had been completed, the simulations were started. Each simulation was run separately to one another, so as to ensure that they would run and complete correctly, and also to not overload the computer actually running the simulations.

Chapter Three: Results from the Two-Stage Light Gas Gun

This chapter will present the results from the experimental shots performed using the two-stage light gas gun, separated into two sections; the first section will deal with the results using the aluminium target set-up, and the second with the soda lime glass target set-up. Table 6 outlines the shot program details including the dates of the experiment, projectile, impact velocity, the impact angle and the target material.

Shot Date	Shot Number	Impactor Material	Impactor Diameter/[mm]	Impactor Velocity/[km/s]	Target Plate Material	Target Configuration Angle/[°]
12/11/2015	G12115/2	Stainless Steel AISI 420	2.00	5.07	Aluminium	90
03/12/2015	G031215/2	Soda Lime Glass	1.98	4.88	Aluminium	90
03/02/2016	G030216/1	Zirconia - Batch 82/8048102 13/03/2009	1.50	4.93	Aluminium	45
11/02/2016	G110216/1	Zirconia - Batch 82/8048102 13/03/2009	1.50	4.57	Soda Lime Glass	45
25/02/2016	G250216/1	Zirconia - Batch 82/8048102 13/03/2009	1.50	4.87	Soda Lime Glass	30
10/03/2016	G100316/2	Zirconia - Batch 82/8048102 13/03/2009	1.50	4.96	Soda Lime Glass	60
11/03/2016	G110316/2	Zirconia - Batch 82/8048102 13/03/2009	1.50	4.88	Soda Lime Glass	60
24/03/2016	G240316/1	Zirconia - Batch 82/8048102 13/03/2009	1.50	5.24	Aluminium	45
24/03/2016	G240316/2	Zirconia - Batch 82/8048102 13/03/2009	1.50	4.85	Aluminium	60
24/03/2016	G240316/3	Zirconia - Batch 82/8048102 13/03/2009	1.50	4.79	Aluminium	30
02/09/2016	G020916/1	Zirconia - Batch 97/4695/03 17/03/16	1.50	4.85	Aluminium	90

Table 6 - Table showing the shot program details. Shot numbers G12115/2, G031215/2 & G020916/1 are the test shots previously mentioned in Chapter 2, Section 2.1.1. Shot G240316/1 is a re-firing of G030216/1 with the change of bumper plate from aluminium to copper. Shots G240314/2 & G240316/3 are the other two aluminium target shots using the copper bumper. Shot G110316/2 is a re-firing of G100316/2.

Table 7 shows measurements made regarding the impact craters, the witness plate secondary ejecta features, the bumper plate burst-through features (for the aluminium targets), and the calculated angle of secondary ejecta from the impact, which will all be discussed throughout this chapter.

Plate Material	Shot Degrees	IS[C] to WP (mm)	IS[C] to Bumper Feature [Top] (mm)	IS[C] to Bumper Feature [Bottom] (mm)
Aluminium	30°	24.5	24.0	12.0
	45°	23.5	19.0	9.0
	60°	22.0	11.0	4.0
Soda Lime Glass	30°	35.5	N/A	N/A
	45°	37.5	N/A	N/A
	60°	56.0	N/A	N/A
Plate Material	Shot Degrees	Base of WP to Base of Tick [Projectile Matter] (mm)	Projectile Secondary Ejecta Angle (Base of Tick) (°)	
Aluminium	30°	32.0	52.561	
	45°	25.0	46.771	
	60°	9.0	22.249	
Soda Lime Glass	30°	53.0	56.185	
	45°	23.0	31.522	
	60°	15.0	14.995	

Table 7 - Table showing measurements made regarding the Impact Site Crater (IS[C]), the Witness Plate (WP), the feature on the copper bumper plates from the aluminium targets (Bumper Feature [Top] & [Bottom], the secondary ejecta pattern on the copper witness plates (Base of Tick [Projectile Matter], and the calculated angle of the secondary ejecta using the data measured.

The data from Table 7 will be further discussed later on within this results section, but an explanation of a few of the terms from the figure follows here:

1. IS[C] to WP – this is the measured distance (in mm) between the centre of impact crater to the witness plate
2. IS[C] to Bumper Feature [Top] is the measured distance (in mm) between the centre of the impact crater to the edge of the bumper feature burst-through ejecta in the same direction as the projectile’s movement (the side closest to the end of the aluminium plate that had the copper witness plate fixed to)
3. IS[C] to Bumper Feature [Bottom] is same as IS[C] to Bumper Feature [Top], but is on the opposite side of the burst-through ejecta (the side of the feature farthest from the copper witness plate)
4. Base of WP to Base of Tick [Projectile Matter] is the measured starting height (in mm) of the projectile secondary ejecta matter on the copper witness plate – this was measured starting from the edge of the witness plate that was next to the aluminium/soda lime glass target when perpendicularly fixed in place was the shot firing

Figures 8 & 9 below show where the described measurements were taken in relation to the crater, the target & witness plates, and the secondary & burst-through ejecta.

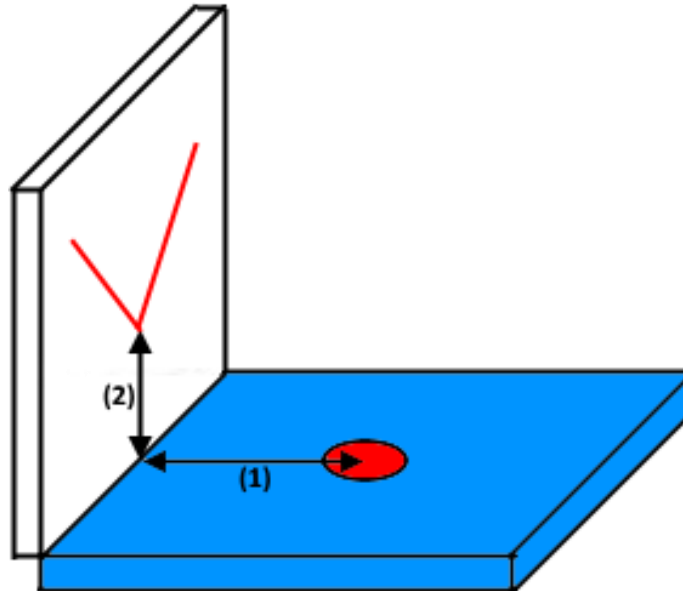


Figure 8 - Illustration showing where the measurements relating to the witness plate were taken. The blue block is the target plate and the white block is the witness plate. The red circle shows the impact crater and the red lines are to imitate the projectile matter within the secondary ejecta pattern. Arrow (1) is the measurement 'IS[C] to WP' and arrow (2) is 'Base of WP to Base of Tick [Projectile Matter]'.

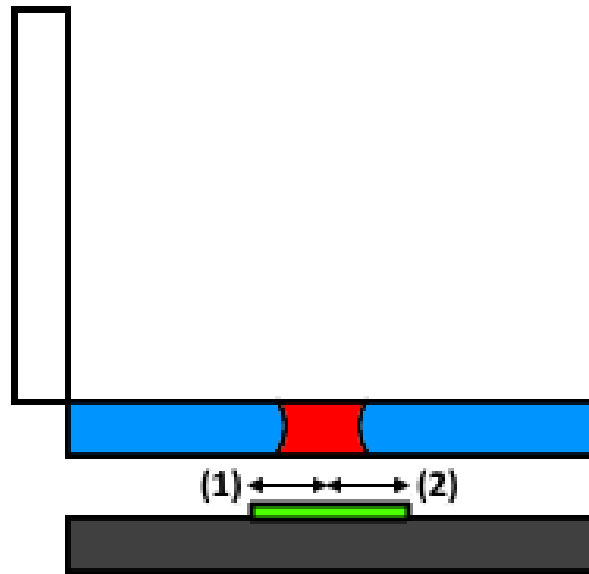


Figure 9 – Illustration showing the measurements relating to the crater and bumper feature. Again, the blue block is the target plate, the white is the target plate and the red region on the target plate is the crater. The grey block below the target plate is the bumper plate, and the green region on this plate is to show the bumper feature burst-through ejecta. Arrow (1) here shows the measurement ‘IS[C] to Bumper Feature [Top]’, whilst arrow (2) shows the ‘IS[C] to Bumper Feature [Bottom]’ measurement.

3.1 Aluminium Targets

This section will deal with the aluminium target set-ups at the three different angles. Discussed here will be the physical findings of the shots, such as the distances between measurable points of the impact sites and secondary ejecta patterns, the appearance of the secondary ejecta on the copper witness plates, and also projectile burst-through information on the copper bumper plates. It will also include analysis using a Scanning Electron Microscope for elemental information from the impacts on both the copper witness and bumper plates, and 3D images of the craters and bumper plates.

3.1.1 30 Degrees – G240316/3

For the 30° shot into the aluminium target, it was seen that, just by the naked eye, the crater formed by the impact had a slight elliptical appearance, slightly stretched in the direction of the projectile’s trajectory. The leading edge of the

crater (the edge of the crater that was in the same direction as the projectile's trajectory) has a more pushed-back, smooth appearance in comparison to the trailing edge of the crater. The trailing edge of the crater has a rougher, torn apart type look; the edge of the crater is a lot more jagged and broken apart, having sharper edges of aluminium visible, opposed to the flatter, smoother looking leading edge. The leading edge seems to have a more rounded appearance of where the aluminium has been pushed up and outwards, whereas the trailing edge has a flatter, but still jagged profile. The crater can be seen in Figure 10.

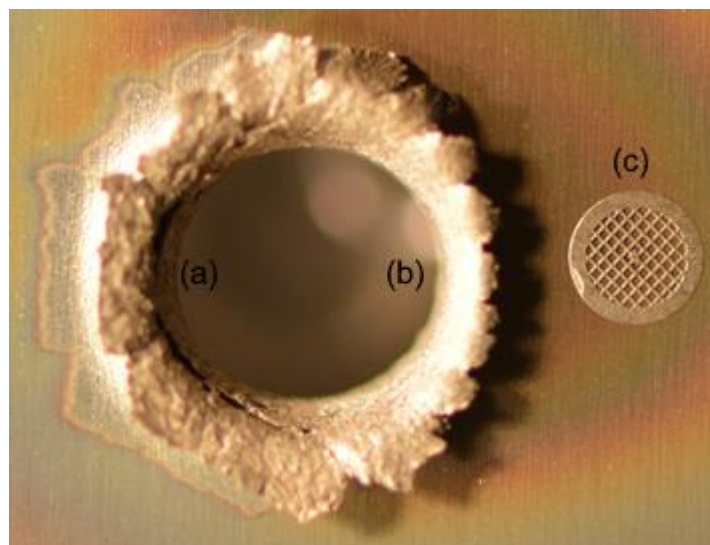


Figure 10 - Image showing the crater formed by a zirconia projectile travelling at a 30° angle in an aluminium plate. The leading edge of the crater is shown by (a), whereas (b) shows the trailing edge. The size marker, (c), is 2.5mm across.

The impact occurred 24.5mm away from the copper witness plate, and it was found, after analysis using a Scanning Electron Microscope, that matter from the zirconia projectile was found within the secondary ejecta pattern (which can be seen in Figure 12) starting at 32mm from the base of the witness plate (all of the measurements can be found in Table 7). After using trigonometry, the projectile matter was found to move away from the impact site at a minimum angle of 52.561°. It was also very apparent that the secondary ejecta had formed an extremely distinct sideways 'V' shaped pattern on the witness plate (later seen to be two distinct 'V' patterns after elemental analysis). The below

figure is an image taken of the copper witness plate, with certain visual markers added.



Figure 11 - Image showing the impact crater (within the black circle) and the copper witness plate with the distinct sideways 'V' shaped secondary ejecta pattern. The red line has been placed to indicate the approximate visual centre of the 'V' pattern, and the white arrow indicates where the projectile matter began within the 'V' pattern (using a Scanning Electron Microscope) from the base of the witness plate.

As stated above, a Scanning Electron Microscope (SEM) was used to analyse the copper witness plates from the experimental shots. Below is a colourised elemental image of the 30° copper witness plate, showing the secondary ejecta pattern, the 'V' pattern central line and projectile matter measurement line.

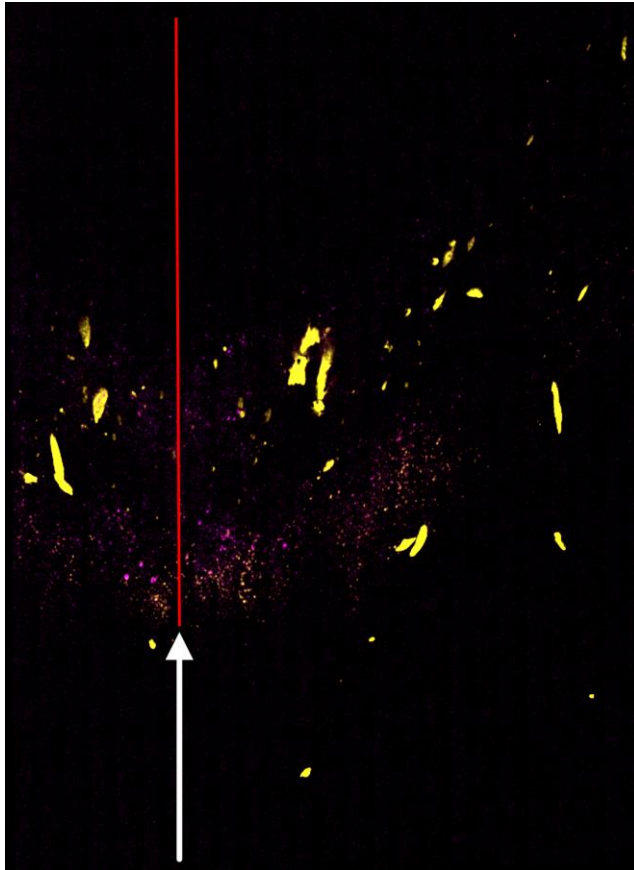


Figure 12 - Colourised elemental SEM image of the copper witness plate with a 50x magnification applied. The pink colour seen in the image is Zirconium, which would only be found in the projectile. The yellow colour is Aluminium, which would be present within the target face plate. The black background is the copper witness plate itself. As seen in Figure 14, the red line has been placed to show the approximate visual centre of the 'V' pattern, and the white arrow shows where the projectile matter can start to be seen (32mm – not to scale) from the base of the witness plate.

The copper witness plates were cut down in size so that they would fit into the SEM for elemental analysis – this is why in Figure 12, the red central line of the 'V' pattern is off centre, and only one side of the pattern can be fully seen (the right side of the red line) with only a small amount of the other side visible (to the left of the red line).

From Figure 12, it can be seen that there seems to be two separate 'V' shaped fan patterns; the lower fan can be seen to have a mixing between fine dust aluminium and fine dust zirconium. This can also be seen to be present on the outside edge of the lower fan pattern on the right hand side. Larger chunks of aluminium are present higher up on the second fan, but can also be seen to a lesser degree on the lower fan – when looking along the arms of fan patterns,

the fine dust aluminium becomes less apparent. The fine dust zirconium on the other hand became more apparent at the centre of the higher up 'V' fan pattern, but can also be seen to be present within the arms of both fans. Unlike the aluminium, no large chunks of zirconium can be seen to have survived the impact within the ejecta pattern, only the fine dust matter.

Looking at the lower down fan pattern, it was found that there seemed to be what looked like large splats of aluminium present, around 200microns in length, with extremely small lumps of zirconium present on top of them. Small craters with a length of around 20.1microns (some even down to 2.34microns long) were also seen in the lower down fan; these smaller craters, as well as the leading edge (same direction as ejecta material) of larger craters were dominated by projectile material, whereas aluminium was seen to be more present within larger craters. Overall, there was not much zirconium present at the very base of the lower down fan pattern, but there was a lot more fine-dust aluminium seen.

On the higher up fan it was seen that there were many small craters, the smallest being around 3.51microns across and the largest around 0.18mm across. In comparison to the lower fan, there were no aluminium splats present, only the large chunks visible in Figure 12, and fine dust seen within in the base of craters. Zirconium was also seen to be present, as small chunks, within larger craters of sizes between 20microns to 60microns across – there were very few craters larger than 60microns across within the higher fan.

At the centre of both of fan patterns, many small aluminium splats and craters were found; the craters were mainly 30microns across or smaller. These two different features were seen to be separate, with many more craters than aluminium splat features. When viewed with a higher magnification, it was found that most craters present were less than 17.5microns across; some were as small as 2microns, with only a few larger than 17.5microns. As seen in the lower fan, the aluminium splat features showed small amounts of zirconium deposited on top of them. Unlike the lower fan, zirconium was not seen present within smaller craters, but aluminium was again seen in the larger craters. It was also noted that some of the aluminium splat features seemed to scrap the

copper witness plate surface, as though the aluminium had come into contact with the plate but stopped moving shortly after the impact.

In Figure 11, some small trails are visible below the centre of the lower down fan pattern. Just as higher up in both of the fan patterns, craters were found present in these areas, but were extremely small, with most being around 6.6microns across, but an extremely small number were measured to be up to around 30microns in size. There was also much less aluminium splatting, with the largest being around 6.6microns long. In addition to the small craters, some even smaller pitting was seen, ranging from 0.4 microns to 1.1microns in size. In this area, there was much less zirconium seen in comparison to aluminium, with the zirconium usually being present on top of the aluminium splats in extremely small chunks and on the edges of the larger craters, where aluminium could also be seen.

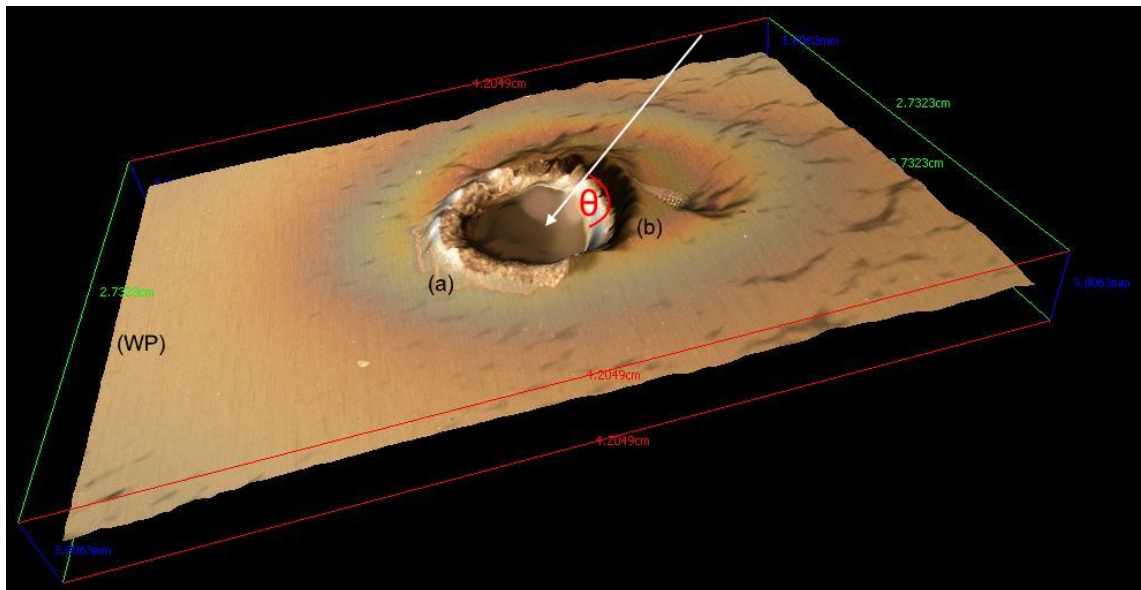


Figure 13 - 3D image created using angle distorted photos of the impact crater formed in the aluminium target plate, where (WP) shows the end of the target plate where the copper witness plate was fixed, the white arrow showing the approximate incoming path of the projectile, θ its incoming angle – in this case, 30°, (a) indicating the leading edge of the crater, and (b) the trailing edge of the crater)

The 3D image seen in Figure 13 was created by using two different photos on the impact crater, one taken directly above, and the second taken by rotating the target plate by 6° clockwise with respect to the camera, with the camera

being at a height of 40.5cm from the target plate. The image was compiled using the MeX software from Alicona (Alicona n.d.) by taking two photographs of the impact site – both with the crater sitting centrally in the camera's views, with one image taken perpendicular to the camera lens and the second image having the plate tilted by 6° . The crater created by the impact can be clearly seen, more easily so at the leading edge, (a), of the crater. It can also be seen that, but to a lesser degree, that the crater has a slight elliptical shape, slightly more elongated in the direction of projectile motion. The leading edge of the crater (b), can be partially seen, but due to shadowing from the lip of the crater overspill when the photos were taken, the edge of the crater and its shadow have become merged, which has created the more obvious peak in the image seen just by the (b) marker, and the large trough following it where the size marker (seen in Figure 13) had been placed on the plate (which is only just visible in Figure 13 due to the crater lip distortion).

Analysis of the copper bumper plate had also been completed to investigate any possible burst-through from the target plate. Figure 14 shows an image taken of the copper bumper plate.

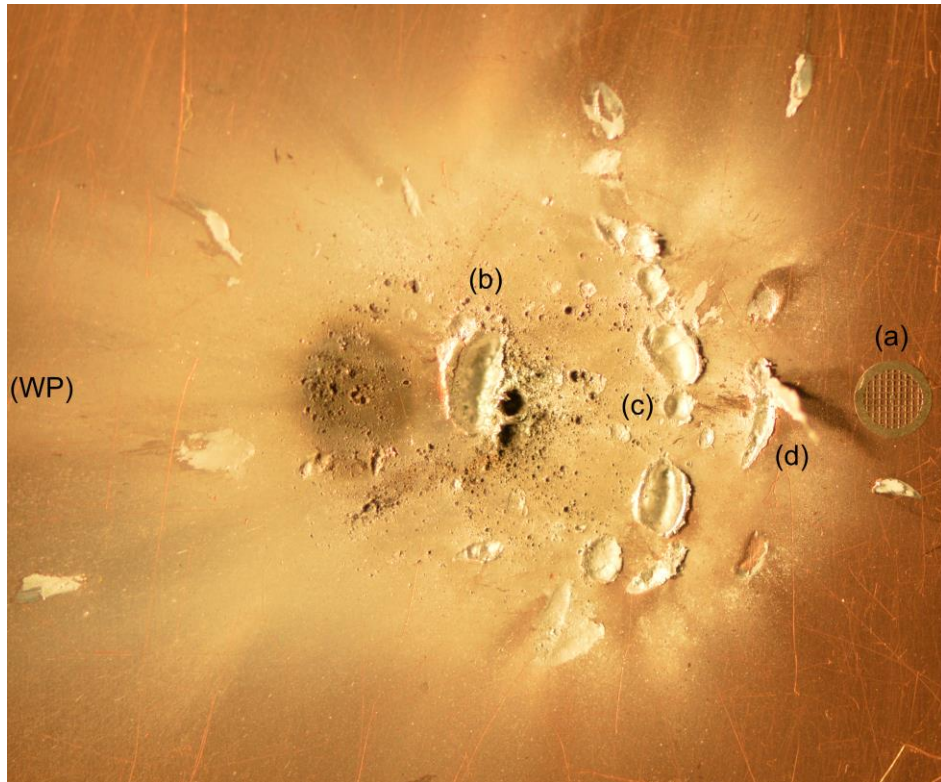


Figure 14 - Image showing the copper bumper plate with burst-through ejecta from the impact. (WP) shows the end of the plate the copper witness plate was fixed to, (a) the size marker (2.5mm across), (b) showing a central crater in the plate, (c) showing more craters in a curved pattern, and (d) shows another crater with a large chunk of aluminium target plate sticking out of it.

As Figure 14 shows the copper bumper plate, it is to be noted that the ejecta was formed below the impact crater seen in Figures 10 & 13. As mentioned in Figure 12, the bumper feature is around 32mm in length (the farthest left hand feature was measured to be 24mm from the centre of the impact crater, and the farthest right hand feature was measured as 12mm from the same point). As can be seen at point (b), a large crater has been formed due to the burst-through ejecta (which can be better seen in Figure 15 below), as well as some more craters in a curved pattern away from the projectile trajectory direction (c). Behind these, marker (d), another crater has been formed, but this crater had a large piece of aluminium sticking out of it, deposited by the impact from the aluminium target plate.

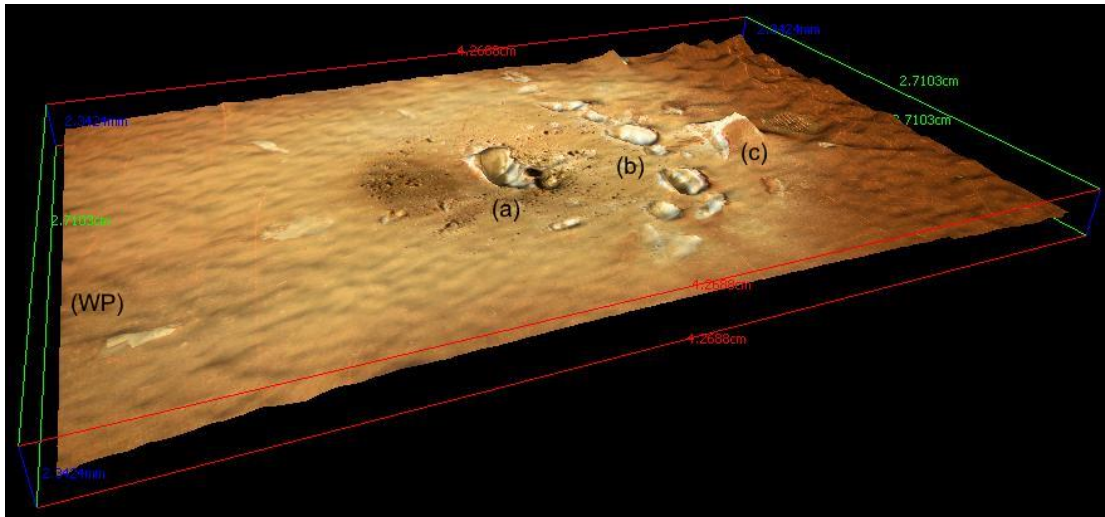


Figure 15 - 3D image showing the burst-through ejecta on the copper bumper plate. (WP) shows the end of the plate where the witness plate was fixed, (a) the central crater, (b) the curved ring of craters, and (c) the crater with the aluminium piece sticking out of it.

The crater seen at points (b) and (c) in Figure 14 can be more clearly seen in Figure 15, points (a) and (b), where point (c), the crater with the aluminium sticking out of it, is more visible, but due to the near-upright profile of the aluminium, the profile of this had merged with the copper plate.

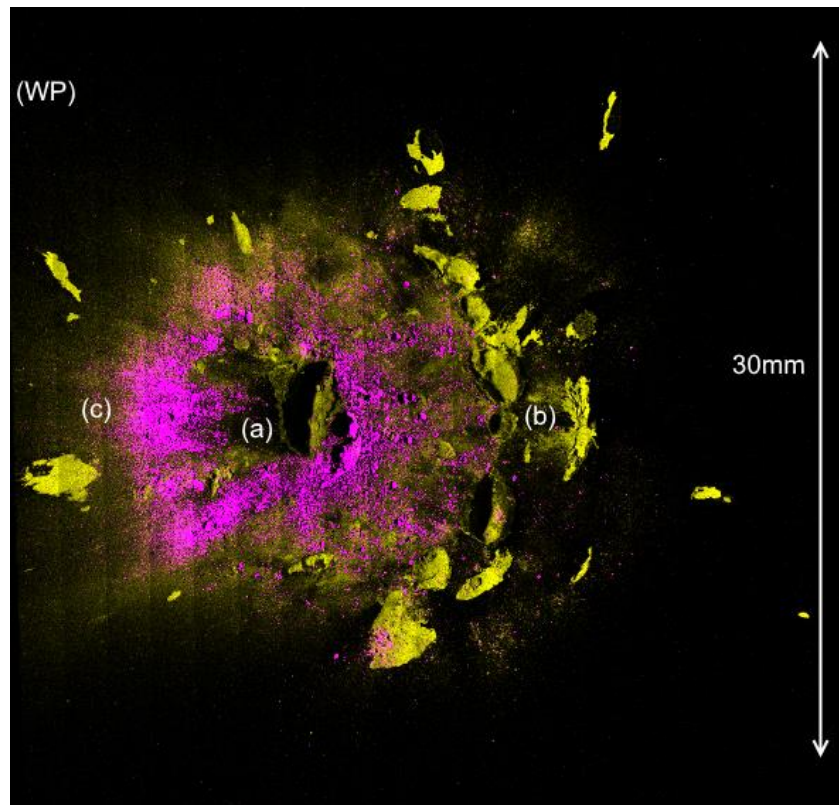


Figure 16 - SEM elemental image of the copper bumper plate. The pink colour again is used to signify zirconium, and the yellow is aluminium. The (WP) marker shows the witness plate end, (a) shows the central crater, (b) the curved craters and aluminium-piece crater, and (c) showing a zirconium-rich area outside of the central crater.

From the elemental mapping see in Figure 16, it is clear that the central crater, (a), and the curved craters, (c), are all dominated by aluminium. Aluminium can also be seen on the outer edges of the bumper feature in both large splats and smaller chunks deposited on the surface, whereas a fine zirconium dust can be seen all around the centre crater, but only inside of the area bounded by aluminium matter.

3.1.2 45 Degrees – G240316/1

The impact crater formed in the 45° shot was seen to have an elliptical shape, but less so than that crater found at 30°. It was also seen that the leading crater edge had a less uniform appearance, with more target plate material intact on one half of the edge than the other. The leading edge (marker (a) within Figure 17) looked to be more pushed-out and bent over in area where more aluminium was still intact, and more broken and sharp looking where there was less. The

outside edges of the crater were both found to have similar amounts of intact aluminium as each other, but more so that the leading edge, as they moved towards the trailing edge of the crater (marker (b) within Figure 17), and the trailing edge itself was seen to have fairly even amounts of intact aluminium, but less so that both the outside edges and leading edge. The trailing edge had a much more pronounced jagged and sharp profile than any of the other crater edges had.

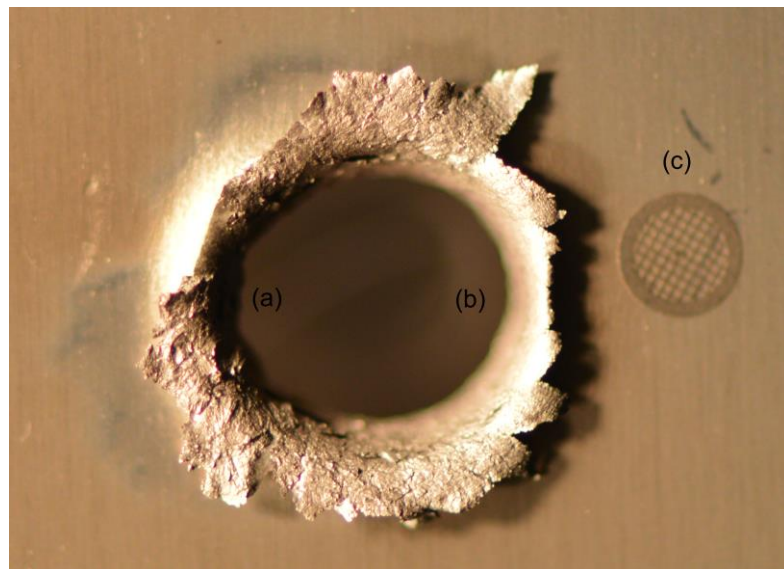


Figure 17 - Image showing the impact crater formed, where (a) is the leading edge of the crater, (b) is the trailing edge, and (c) is the 2.5mm across size marker.

It was measured that this impact occurred 23.5mm away from the copper witness plate, and that zirconium projectile matter was found within the secondary eject pattern starting at 25mm from the base of the copper witness plate. This means that the projectile matter moved off from the impact at a minimum angle of 46.771° . The secondary eject a pattern noticed after this impact was again seen to be in a distinct 'V' shaped fan, but after elemental analysis, it was seen that three separate fans were visible.

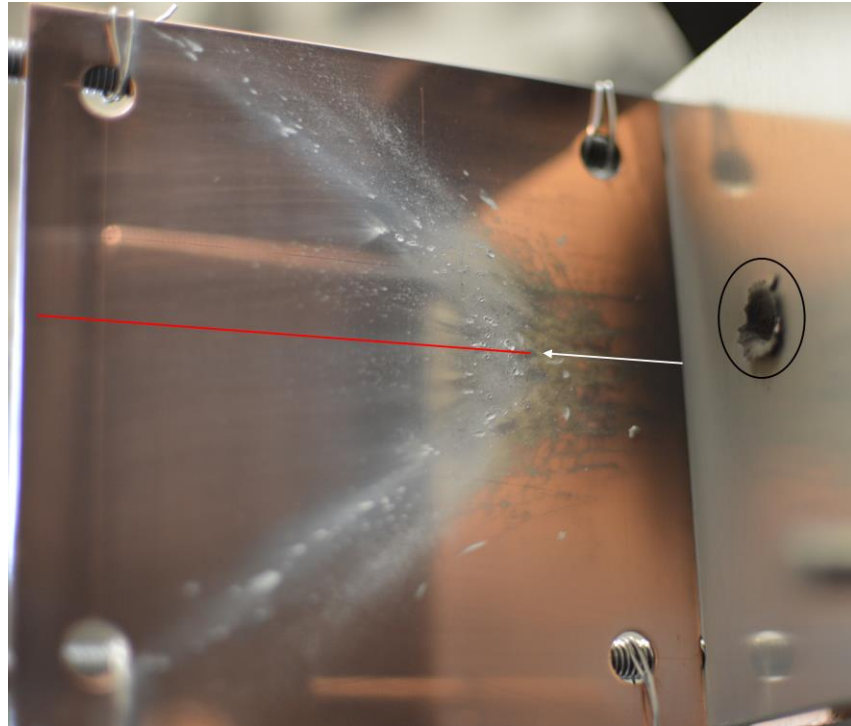


Figure 18 - Image showing the impact crater (within the black circle) and the secondary ejecta fan pattern formed during the impact. The white arrow shows where the projectile material was found at its lowest point within the fan (25mm from the base of the plate), and the red line indicating the centre of the fan pattern.

Elemental mappings of the witness plate were carried out to find out the spread of projectile and target plate matter within the ejecta pattern which can be seen in the following image.

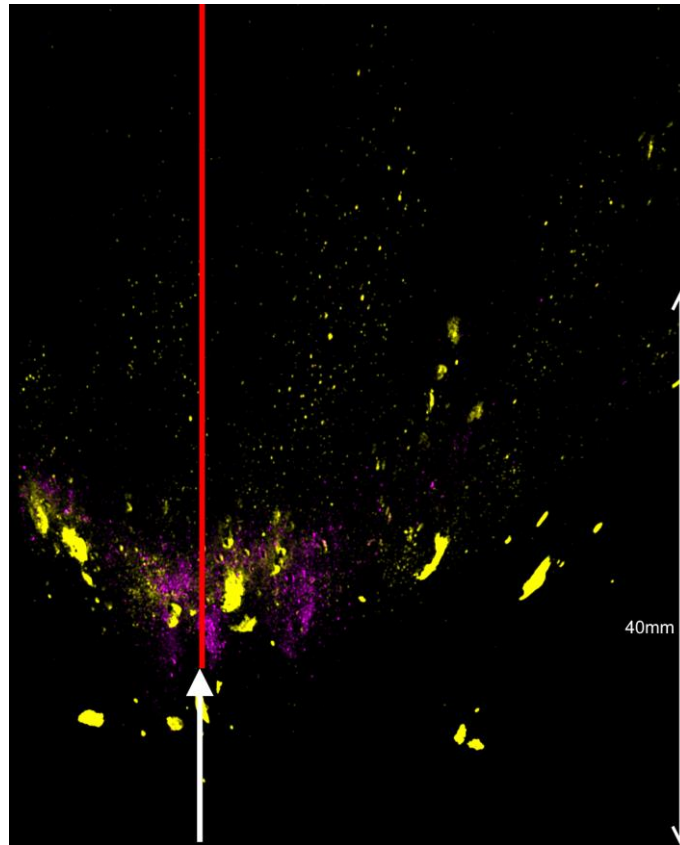


Figure 19 - Colourised elemental image of the secondary ejecta pattern. Pink has been used to show zirconium, whilst the yellow has been used for aluminium. The red line again shows the approximate central line of the ejecta pattern, and the single-headed white arrow shows the starting location of the zirconium matter within the pattern, measured to be 25mm from the base of the plate.

From Figure 19, it can be seen that the ejecta pattern seems to split into three separate fans; the lower two seeming to be very close to each other, but splitting outwards from one another as they move away from the central red line, and the third is a lot higher up in comparison, with the edges of the fan much steeper than the other two. There is more separated fine dust aluminium and zirconium at the centre of the fan patterns, with only a small amount of mixing, with some larger chunks of aluminium present, but only seen in the lowest fan pattern, and in the area below the fine dust zirconium.

When looking more closely at the lowest fan, it was found that there were many aluminium splat features present, seen to have small chunks of zirconium deposited on top of them. There were not many craters seen in comparison to splats, with the largest craters being around 0.18mm in size, but the majority

were seen to be between 0.012mm and 0.036mm in size. As said, the splat features were aluminium based with zirconium chunks on top; the zirconium was only seen on either the leading or the trailing edges of the splats, it was never seen to be in both places on the same splat. Some even smaller craters were seen, ranging in size between 3.51microns to 10.5microns long. Most of these smaller craters were dominated by aluminium, only a small number contained zirconium.

Looking more closely at the middle fan pattern, many small craters were again seen with the majority of them being around 23.4microns long, but some as small as 4.68microns were noticed. As similar to the lowest fan pattern, there were some aluminium splat features, but less than was seen in the lower fan; the splats also featured less zirconium on top of them, with the zirconium rarely being seen on the leading edges of the splats, only mainly appearing on the trailing edge. Zirconium was also more present in craters down to a size of 16microns than aluminium was.

When analysing the highest fan pattern, it was seen that there was considerably less craters and splats than the two lower fans had featured, with one splat seen to be around 0.66mm long, whereas the majority were about 0.054microns across. The splat features comprised of even less zirconium chunks than previously seen, but they were again seen to be present more on the trailing edges of the splats. In other places where zirconium was seen, it had a mixing of dust like particles with smaller chunks, but there were more random areas of only dust like zirconium present. In areas away from the splat features, there was no dust like/chunk mixing seen as there had been much lower down in the centre of the tick.

The centre of the fan patterns was found to have a large number of craters, ranging in sizes between 0.012mm to 0.6mm in length. Unlike the arms of the fan patterns, there were no aluminium splats visible in this area. The craters seen had a higher proportion of aluminium within them, but some did have zirconium present, and a few even had mixing of both materials. The majority of craters had a steep trailing edge, with a flatter and smoother leading edge, where aluminium could be found higher up on the smoother leading edges in

some craters. There was also extremely fine pitting seen within the central area at much higher magnifications.

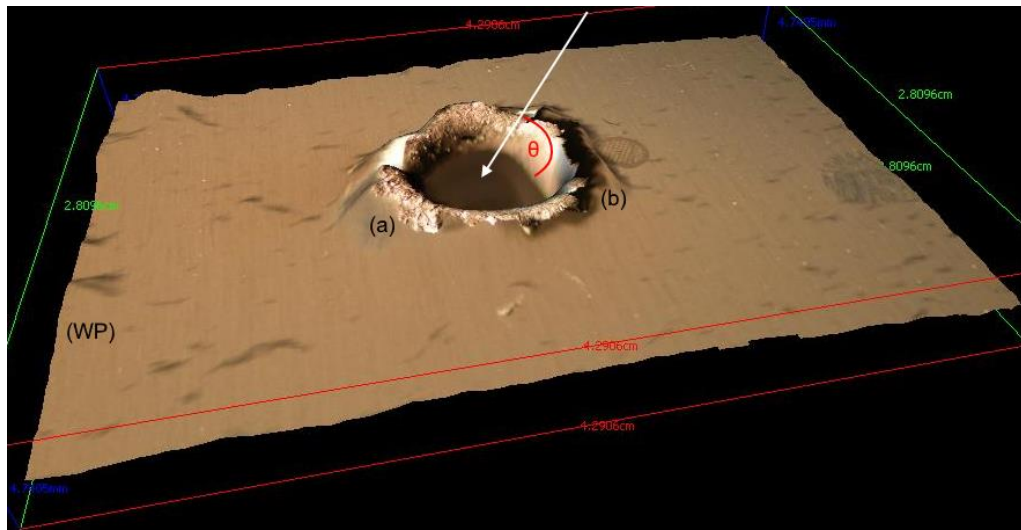


Figure 20 - 3D image of the impact crater, where (WP) shows the witness plate end of the aluminium target, (a) is the leading edge of the crater, and (b) is the trailing edge. The white represents the approximate path of the incoming projectile, and θ shows the angle, which here is 45° .

Looking at Figure 20, the difference in shape of the leading edge can be seen; the part nearest the marker (a) seems to be longer, and more bent over, whereas the top portion on that lip seems to stop quite suddenly, appearing jagged and broken in appearance. The outside edges both seem to be pushed outwards and upwards from the impact crater in a fairly even appearance. The trailing edge, marker (b), looks to have a very steep incline, but also seems to be fairly flat, but sharp, when looking at the edge of the crater lip (this image has again been distorted due to crater lip/shadow overlapping, but this shape and pattern can be seen more clearly in Figure 17).

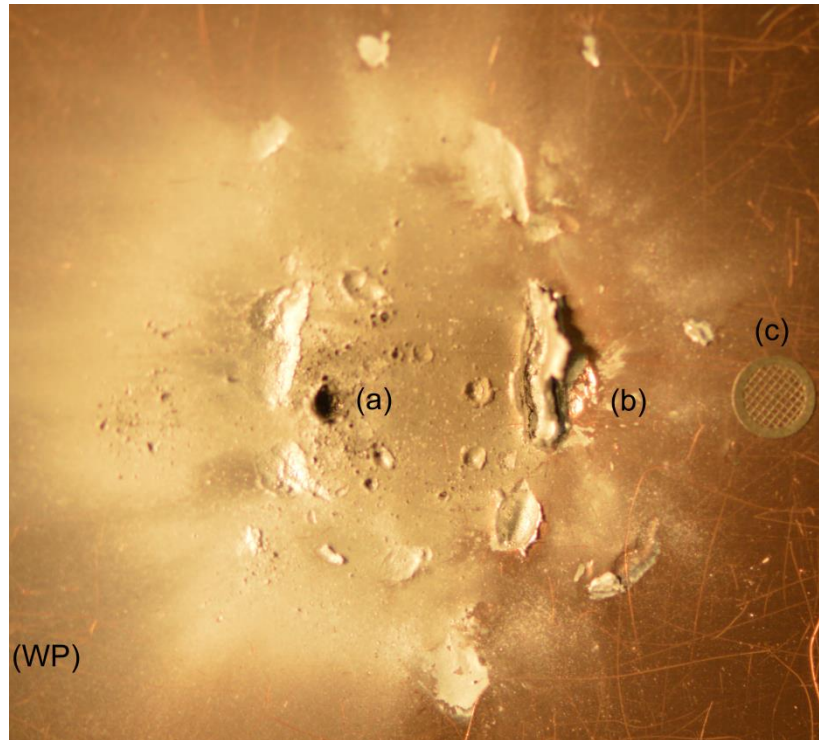


Figure 21 - Image showing the bumper plate burst-through ejecta. The (WP) marker shows the end of the plate where the witness plate was fixed, (a) shows a central crater with smaller pitting around it, (b) shows a slightly curved crater ring, and (c) shows the 2.5mm size marker.

Figure 21 displays an image taken of the burst-through ejecta from the hypervelocity impact. The burst-through ejecta was around 28mm in length (from left to right) as the farthest features measured from the centre of the impact crater were 19mm to the left of the feature in the image, and 9mm to the right (the top and bottom of the feature – explanation and values seen with Table 7). The marker (a) shows a small crater with very small pitting surrounding it, and two larger gouges are visible on the witness plate side of the crater. At marker (b), a large piece of aluminium had become lodged within the surface of the copper witness plate, sticking out nearly perpendicular to the plates surface (it was assumed that the piece was aluminium due to its colour, but SEM analysis confirmed this assumption).

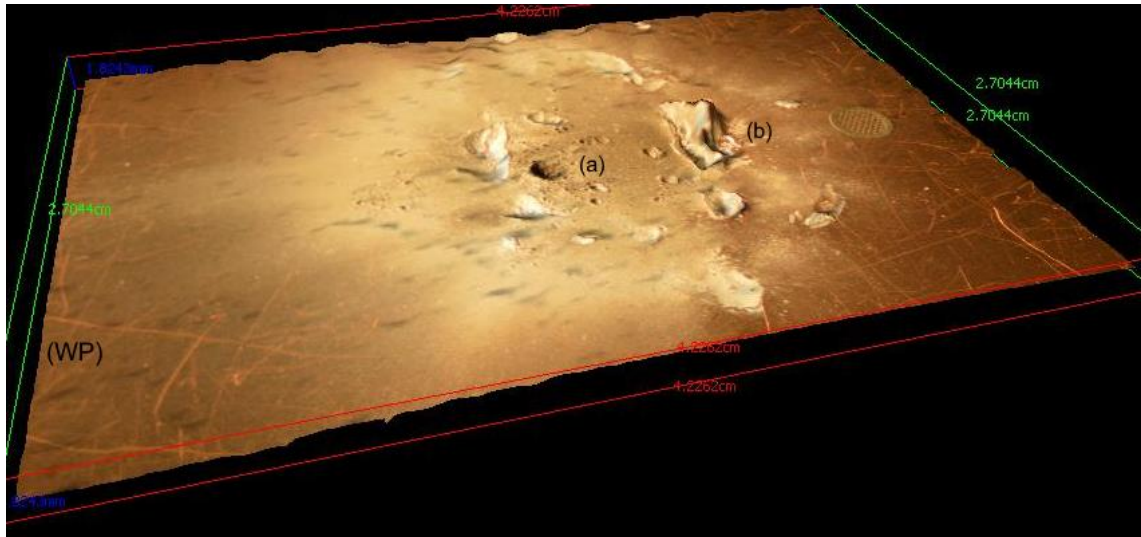


Figure 22 - 3D image showing the burst-through ejecta on the copper bumper plate. (WP) shows the witness plate end of the target, (a) shows the small central crater, with (b) showing the large gouge with aluminium sticking out of it

The central crater and surrounding pitting and gouges can be seen a lot more clearly at point (a) of Figure 22, and the aluminium piece sticking out of the copper surface at point (b) can also be easily seen, including the gouge the aluminium made when it came into contact with the copper, and also the slightly curved alignment of the surrounding craters. The below figure is an elemental map showing the aluminium and zirconium distributions.

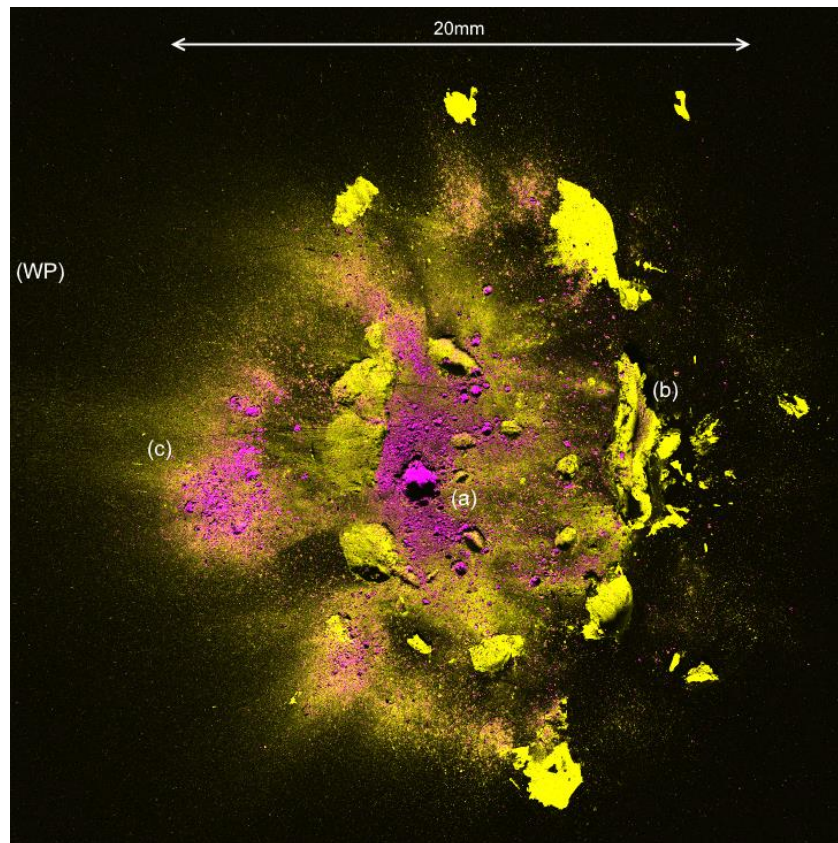


Figure 23 - Colourised elemental image of the copper bumper plate. Pink has been used to colour zirconium, and yellow is used for aluminium. (WP) once again shows the witness plate end of the target, (a) shows the central crater, (b) the aluminium shared gouge, and an area originally unknown to contain any projectile and target matter is shown by (c).

At point (a) in Figure 23, the central crater and fine pitting very nearby is dominated by projectile material, and the larger craters around this area have a much higher concentration of aluminium present, just as most of the larger craters do within the figure, regardless of closeness to the central crater. The projectile matter seen within the central area also has a slight curved nature to it as it moves away from the central crater (upwards and downwards in Figure 23). As mentioned before, the feature seen in [Figure 21 (b)] and [Figure 22 (b)] was confirmed to be aluminium, seen as marker (b) in Figure 23. This shard of aluminium was also noted to have small chunks of zirconium present on it, as did the aluminium-dominated gouge that the shard had made in the copper plate. The surrounding, elliptically-aligned craters also have the same elemental features as [Figure 23 (b)], only that they do not have any kind of aluminium shard present within their crater limits. The only other place that projectile matter was seen, in large concentrations and not small chunks, away from the

central crater was at point (c). Here it can be seen that there is a small amount of mixing between fine dust aluminium and fine dust zirconium, but mainly it seems that the zirconium is present on top of the aluminium in this area, as the area around this has considerable amounts of fine dust aluminium, as it would make sense that the zirconium dust settled after the aluminium dust had made contact with the plate, this being that the zirconium may not be as visible if it had not.

3.1.3 60 Degrees – G240316/2

The crater formed in the 60° shot had a much more pronounced ‘egg-type’ shape; the leading edge of the crater came more to a point, whereas the trailing edge had a flatter, rounded appearance. The lips of the crater were, if mirrored horizontally in Figure 24 through the centre of the image, a lot more symmetrical than previously seen with other angled shots. The lip all the way around the crater also seems to have a fairly uniform appearance, looking quite peeled-back and more jagged and sharp all the way around the lip as opposed to just one portion looking that, such as the leading edge, and the trailing edge looking different.

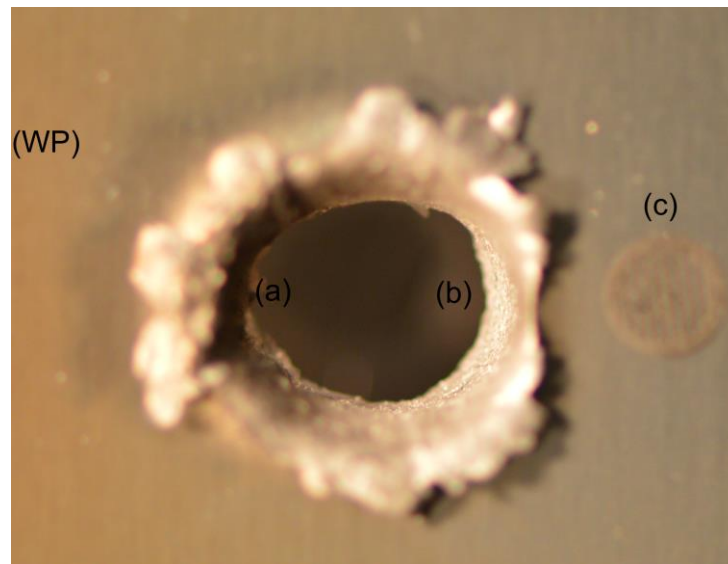


Figure 24 - Image showing the 60° impact crater. (WP) marks the side of the plate where the witness plate was attached, (a) and (b) the crater leading and trailing edges respectively, and (c) is the 2.5mm size marker.

This impact occurred 22mm away from the copper witness plate, and the first sightings of projectile material on the witness plate were 9mm from its base. This would mean that the projectile material travelled with a minimum angle of 22.249° away from the impact site. Similar to the previous two shots, the secondary ejecta pattern was again in the familiar 'V' shaped fan, obviously this time a lot lower down on the witness plate, with the fan itself having a more open, obtuse appearance; this can be seen in the following figure.

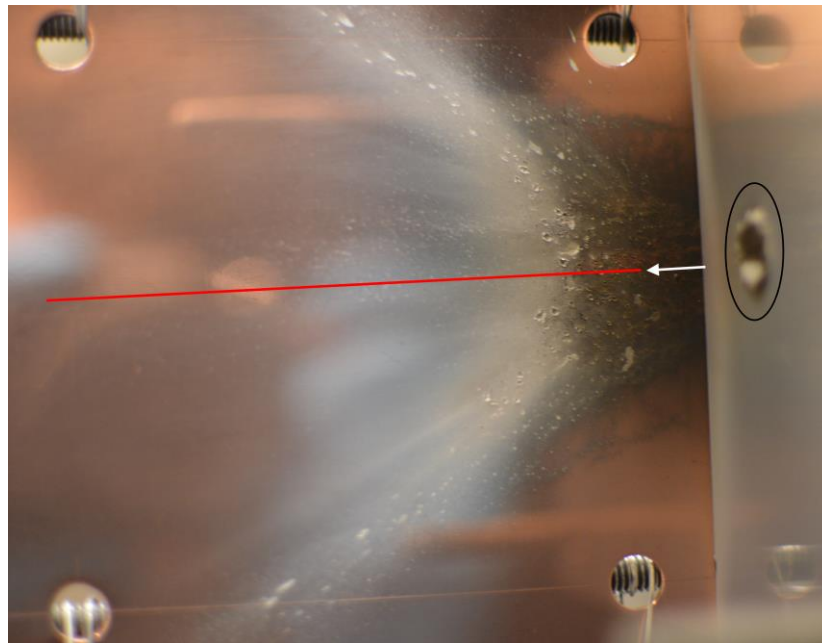


Figure 25 - Image taken of the secondary ejecta pattern on the copper witness plate. The impact crater can be seen in the black circle, the white arrow shows where the projectile matter began within the ejecta pattern, and the red line shows the approximate centre of the 'V' pattern.

It can be seen in Figure 25 that the ejecta pattern is considerably lower down the copper witness plate, even though the impact site is not that much farther away, or closer to, the witness plate (see Table 7 for measurements). This secondary ejecta pattern can also be seen to have what appears to be a fairly well defined 'V' shape fan; it can be seen starting with the white-dust areas that have the line of craters within it, extending outwards and ending with the area of more diffuse spray of smaller craters. Along the red line in Figure 25, a thin region of fine splatting can be seen (though this was only seen after SEM analysis, it was first believed to be cratering) that extends upwards from the

centre of the fan, and a wide area of craters is also visible below the centre of the fan, close down to the witness plate base.

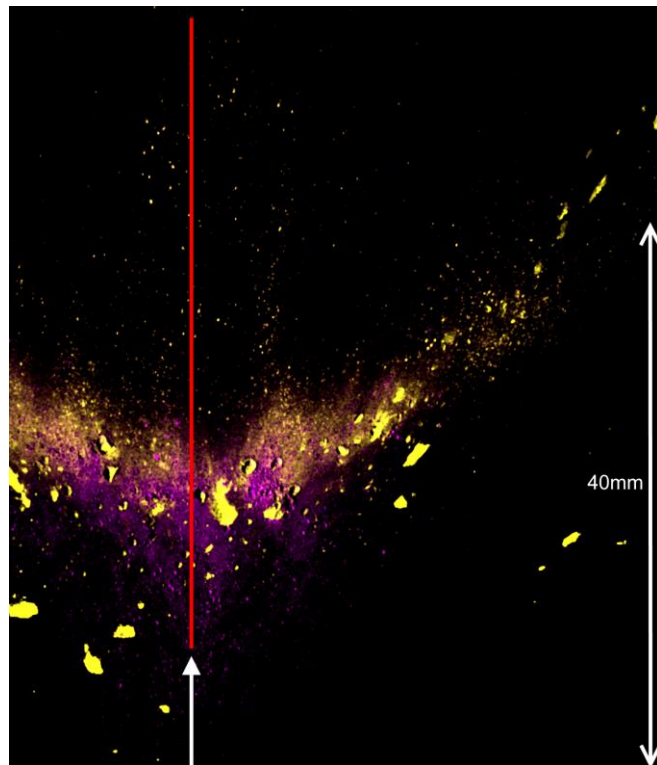


Figure 26 - Colourised elemental image of the secondary ejecta pattern. The single-headed white arrow shows where the majority of the projectile matter started within the pattern, and the red line shows the approximate centre of the fan pattern. Pink was again used for the zirconium, and yellow for the aluminium.

After the SEM elemental image was obtained for the secondary ejecta pattern (Figure 26), the defined fan shape of the ejecta was even more evident. A fan arm can clearly be seen extending outwards from the central area of fine dust zirconium, where the arms are made up of both dust like and small chunks of aluminium, and some dust like zirconium for a third of the way up. There is only a small amount of mixing between the dust like aluminium and zirconium, and this can be seen on the insides of the fan arms, from the centre of the fan pattern to approximately half the way up the arm.

On the lower down, outside portion of the fan arm, small pitting and cratering were observed, with the smallest being around 0.06mm across (which were most abundant), and the largest around 0.12mm across; some craters were even seen down to sizes of around 3.51microns across. There were many

aluminium splat features seen, with the most seen of all the three angle witness plates. The features had a much more elongated trunk with as much more rounded trailing edge, and the splats still had the small zirconium chunks present on top of them, but there was less zirconium than seen previously.

Higher up on the inside edge of the fan pattern, around halfway up the arm, there were less craters and splats seen – the largest craters seen were around 0.03mm in size with the majority being smaller, and the largest splat was around 0.1mm long, though again the majority were much smaller than this. The aluminium splats kept their previously seen shape of a rounded trailing edge and longer trunks, and the zirconium was still present on them, but even less than seen on the same witness plate in a different place. Both zirconium and aluminium were present within craters (zirconium more present within craters than on splats), where the zirconium was seen more inside of the craters, and the aluminium present on the edges of the craters.

When analysing the higher up central area in the middle of the fan arms, many small aluminium splats were found. Their sizes ranged from 30.4microns to 0.3mm in length, and they again had the rounded end/long trunk look seen. The zirconium chunks were more even distributed among the aluminium splats, but the overall amount of zirconium was lower than previously seen; this being said, the amount of dust like zirconium increased, with most being seen around the aluminium splats.

Within the centre of the 'V' pattern, it was found that there were no aluminium splats, and that crater numbers & pitting dramatically increased; the size of the craters seen were mainly between 0.018mm and 1.2mm in length, though some outside both ends of the range were seen. Aluminium was present around the lip edges of craters, with zirconium detected within the craters – the aluminium had an overall dust like, evenly diffuse appearance in this area, whereas the zirconium was more concentrated in particular places. Some craters, with a diameter of around 9microns (and only of around this size), were seen to have what can best be described as small trails leading away from them, where the trails had lengths of around 14microns. These trails seemed to be made up of both aluminium and zirconium, with a higher amount of aluminium present

within them. It must be said that these small trails had not been seen anywhere else, on any other craters, for the aluminium targets witness plates; they were only present for to central area of the fan pattern for the 60° experimental shot.

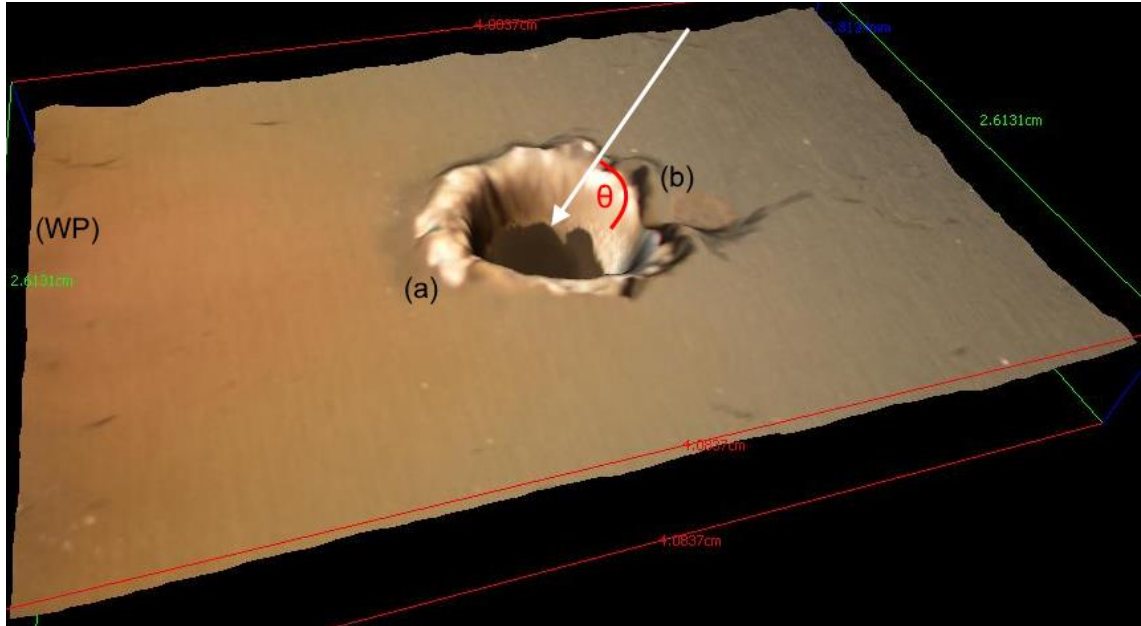


Figure 27 - 3D image of the impact site on the aluminium target plate. (WP) shows the witness plate end of the target, (a) is the crater leading edge, (b) is the crater trailing edge, the white arrow shows an approximate trajectory for the projectile, and the red θ shows the projectile's incoming angle, which in this case was 60°. Due to the shadowing created by the crater lips, and the images being slightly out of focus, the 3D profile of the impact crater is slightly distorted – this can be seen just by the (b) marker, and also on the lower edge of crater between the (a) and (b) markers.



Figure 28 - Image showing the burst-through ejecta with a small chunk of aluminium sticking out of copper witness plate at marker (a), and the 2.5mm size marker, (b).

The burst-through ejecta from the hypervelocity impact shown in Figure 28 is much smaller in size when compared to that of the 30° and 45° burst-through ejecta; the main ejecta feature is only 15mm across (calculated using the measured end positions from the crater centre seen in Table 7). With the naked eye, the main features include a silvery-white dust on the surface of the copper plate, and a small piece of aluminium sticking out of the surface, smaller but similar to that seen on the 45° bumper plate – this piece was again assumed to be aluminium due to the colour, but analysis from the SEM confirmed it.

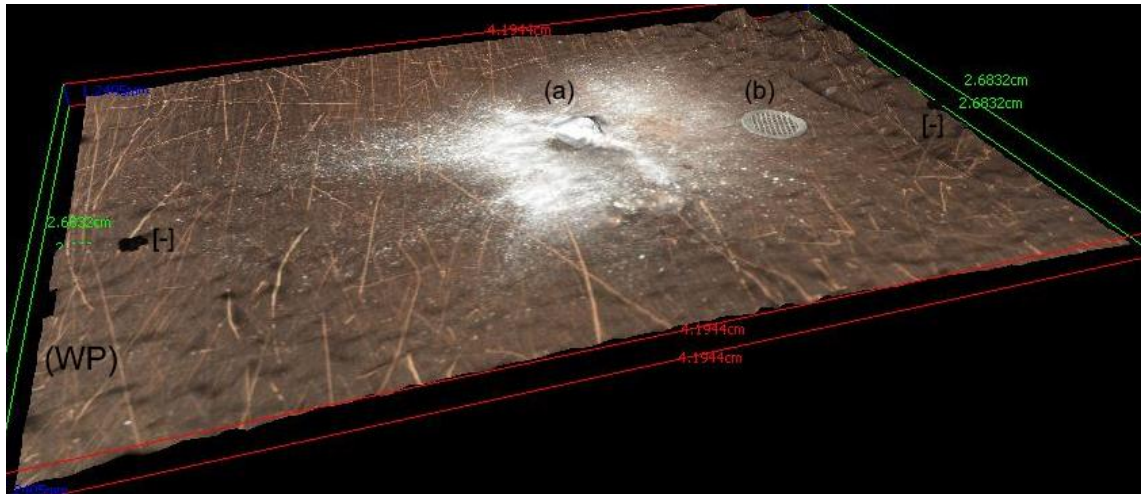


Figure 29 - 3D image of the burst-through ejecta on the copper bumper plate. (WP) shows the end of the plate where the witness plate was attached, (a) is the centre of the ejecta feature, and (b) is the 2.5mm size marker. The two black dots marked by [-] on the copper plate are not part of the ejecta pattern, but are dots made by a marker pen to ensure the correct spatial area was analysed using the scanning electron microscope.

The material lodged within the copper witness plate's surface can be seen just below the (a) marker on Figure 29, with a smaller bump just to the left of it. The rest of the burst-through ejecta can be seen to be fairly flat in comparison to these two features. The colourised SEM image of the ejecta feature (the following Figure 30) reveals quite plainly what the elemental make up was of both the silvery-white dust and the protruding material.

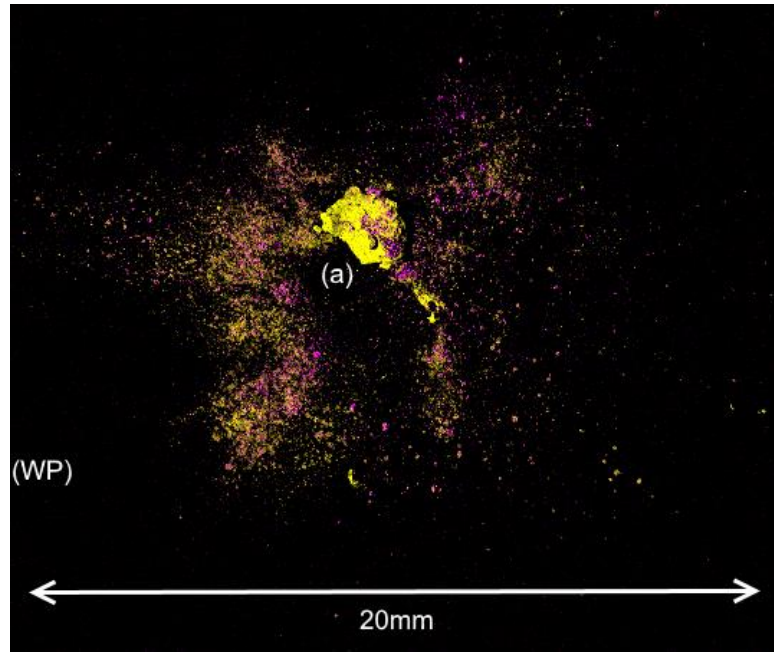


Figure 30 - Colourised elemental image of the burst-through ejecta on the copper witness plate, where (WP) shows the witness plate end of the target & bumper plate, and (a) the central burst-through ejecta feature. Pink has been used to colour zirconium, whilst aluminium is in yellow.

As previously mentioned, Figure 30 clearly shows that the material protruding from the surface of the copper plate was in fact a piece of aluminium from the target plate. The silvery-white dust seen in Figures 28 & 29 is a mixture of fine dust aluminium and zirconium, with some slightly larger chunks of zirconium present, mainly on the aluminium shard, but also seen scattered throughout the fine dust mixture. There are no areas of singularly defined projectile or target plate material like that which was seen with the 30° and 45° burst through ejecta; the aluminium and zirconium are mixed together within the ejecta pattern, apart from the protruding aluminium chunk. Also unlike the 30° and 45° copper bumper plates, there are no obviously detectable craters or pitting on the surface of the bumper plate, only that which was made by, and is at the base of, the aluminium shard when it became lodged within the copper surface.

3.2 Soda Lime Glass Targets

This section will present the results from the soda lime glass target set-ups for the three different angled configurations. Shot G110316/2 is a re-firing of shot G100316/2, and only the results for shot G110316/2 will be included here.

Discussed here will be the physical findings of the shots, and the appearance of the secondary ejecta on the copper witness plates. It will also include analysis using a Scanning Electron Microscope for elemental information from the impacts on both the copper witness and bumper plates, and 3D images of the craters and bumper plates.

Physical measurements and elemental analysis using a Scanning Electron Microscope of the secondary ejecta patterns will be presented and discussed here, along with discussions of the physical appearance of the impact craters formed during the hypervelocity², and a variety of 2D & 3D images; the 2D images will be of the craters and of the copper witness plates displaying the ejecta patterns, whilst the 3D images will show the impact craters in the soda lime glass target blocks. Unlike the aluminium targets, there are no copper bumper plates to be analysed for the soda lime glass targets. This is because the glass blocks did not undergo any complete penetration from the hypervelocity impacts; the projectile matter (and dislodged target matter) either deposited onto the soda lime glass target, or moved away from the impact site and became part of the secondary ejecta pattern on the copper witness plate.

3.2.1 30 Degrees – G250216/1

The impact craters for the soda lime glass targets is drastically different compared to those craters found on the aluminium targets. Seen in Figure 31 below, the area of the soda lime glass outside of the crater boundary (shown by the black circled with the (a) marker) had shattered; the impact had nearly caused the entire glass block to shatter to pieces – Figure 32 shows the extent of the shattering of the glass block. The leading edge of the crater, (c), can be seen to have a small amount of material dislodged from the glass block due to the impact, whereas the trailing edge, (d), has a considerable amount more material dislodged. It was also seen that the wall of the crater's leading edge was steeper than that of the trailing edge's wall.

² Note regarding the lack of elemental analysis of the soda lime glass target craters – There was a fear that, when undergoing the vacuuming process within the Scanning Electron Microscope prior to elemental analysis, that some parts of the shattered soda lime glass block may become dislodged or break free from the target and could either damage itself further, or damage the inner workings of the SEM. It was due to this that the decision was made not to attempt elemental analysis of the craters.

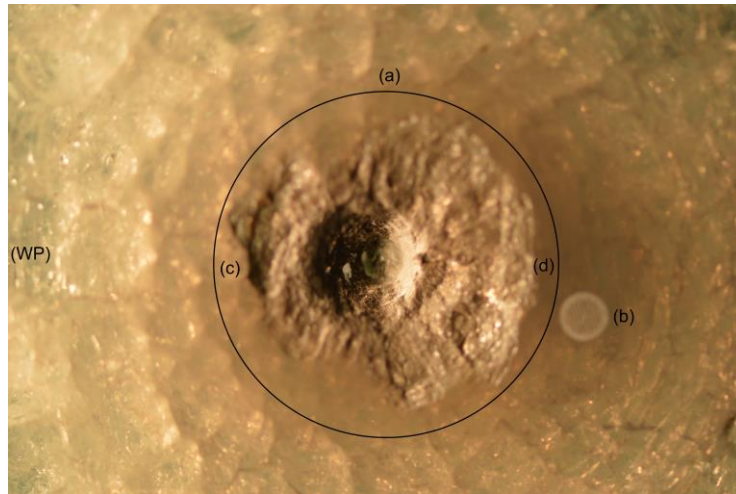


Figure 31 - Image showing the crater formed in the soda lime glass target, where (WP) is the end of the block where the witness plate was fixed, the circle (a) is the crater boundary, (b) is the 2.5mm size marker, (c) is the crater's leading edge, and (d) is the crater's trailing edge.

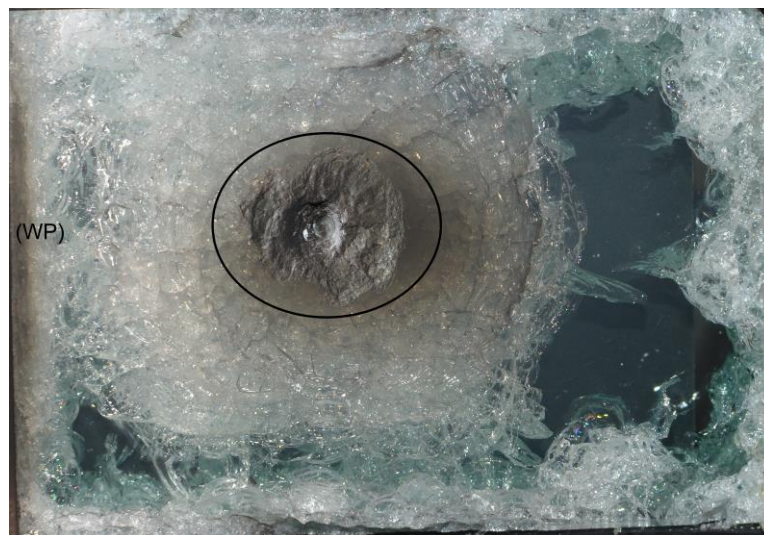


Figure 32 - Photo showing the extent of the glass block shattering post hypervelocity impact. As before, (WP) shows the witness plate end of the target, and the impact crater is bounded by the black ring.

The impact occurred 35.5mm away from the witness plate, and the first sightings of zirconium were seen (after elemental analysis) at 53mm from the base of the witness plate; this means that the projectile matter travelled away from the impact site at a minimum angle of 56.185° . To the naked eye, the ejecta pattern had the previously seen 'V' shaped fan look, but it also had what looked to be trails leading upwards from the base of the plate towards the fan

shape, and also an area above and within the fan arms that was littered with small craters.

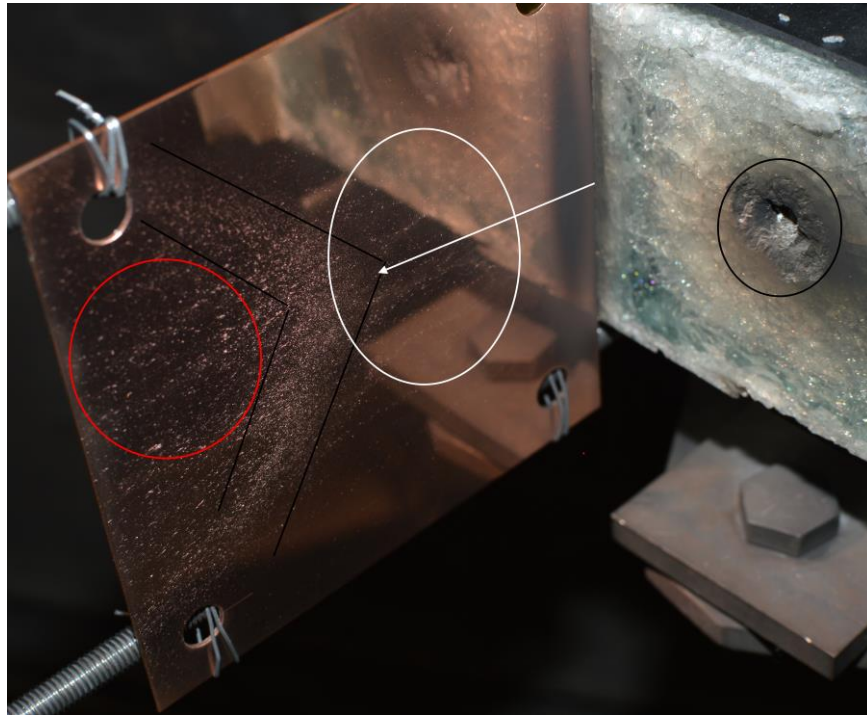


Figure 33 - Image of the copper witness plate and secondary ejecta pattern. The black circle bounds the impact crater, the white arrow showing the approximate height of the first sighting of zirconium within the pattern, the white circle bounds the area of the trails leading from the plate base to the fan pattern, the black lines bound the 'V' fan pattern, and the red circle bounds the area of cratering seen above and between the fan arms.

The following figure is a colourised elemental image taken from the Scanning Electron Microscope of the secondary ejecta pattern.

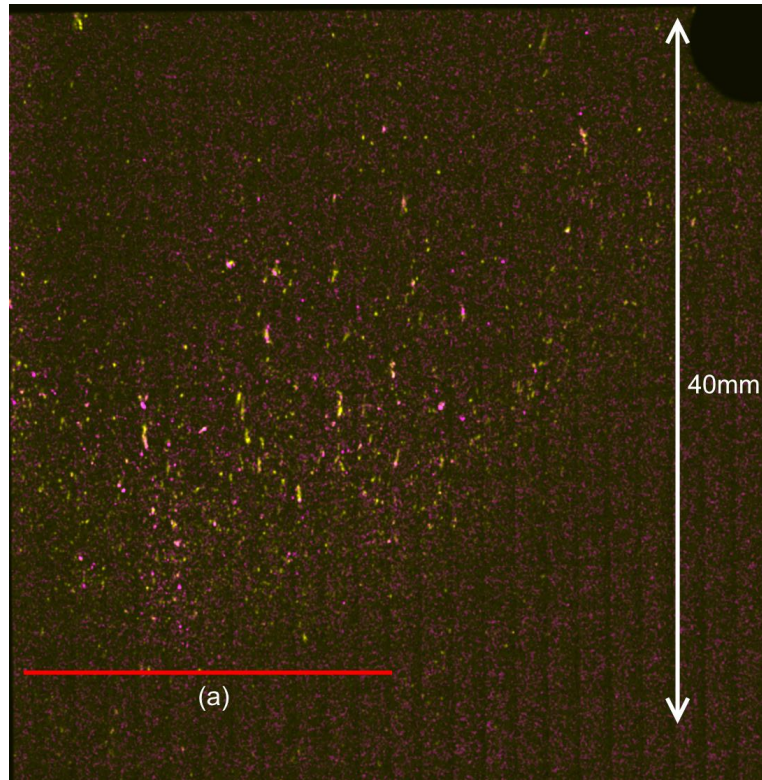


Figure 34 - Colourised elemental image of the secondary ejecta pattern. Pink is used to show the zirconium, whilst yellow is used to show silicon. The red line marked (a) is the marker used for measuring the height of zirconium first seen within the pattern from the base of the witness plate.

Although seen extremely faintly, the 'V' shaped pattern is still present within the secondary ejecta on the copper witness plate, as evidenced by the elemental map in Figure 34. The elements chosen to look for during the analysis on the soda lime glass target experiments were zirconium, which would show evidence of projectile material, and silicon, which would show evidence of target plate material. The majority of the fan seen in Figure 34 is a diffuse mix of fine dust like zirconium and fine dust like silicon, except where silicon seems to be more dominant on the outside base of the fan arm, and zirconium seems to be slightly more abundant towards the centre of the fan.

When looking more closely at the upper portion of the fan arm, a few small splats of silicon could be seen; these splats were similar to those produced by the aluminium during the aluminium target shots. The largest of these splats seen was around 428microns long, but the majority were much smaller, ranging from 28.8microns to 75.3microns in length. These small splats did not show much zirconium at all; zirconium was mostly seen on the leading crater lip

and wall of small craters, the majority being around 19.7 microns long, with some seen to be up to 30.7 microns in length.

When analysing the central area of the fan arms, many craters were seen, some as small as 11.3 microns across, whilst some were nearly 138 microns across. Within this area zirconium was again found to be present within small craters, and chunks of it were also found to be mixed slightly with some larger chunks of silicon – but, there was still not a considerable amount of mixing.

The final area analysed more closely was the area below the fan arms that seemed to have trails present. The trails were made up of lines of small craters, where the largest seen was 180 microns across and the smallest was around 11.3 microns – the majority of these craters were just above and below 30 microns in size. Many of the craters on the larger side had evidence of silicon within them, whereas smaller craters had some zirconium on the craters lips. Some extremely fine pitting was also noticed between the craters, with some of the smallest pitting being 1.14 microns in size – despite the smaller craters having zirconium present, the fine pitting had silicon present within some of the smaller noticed pits, and almost no zirconium nearby at all.

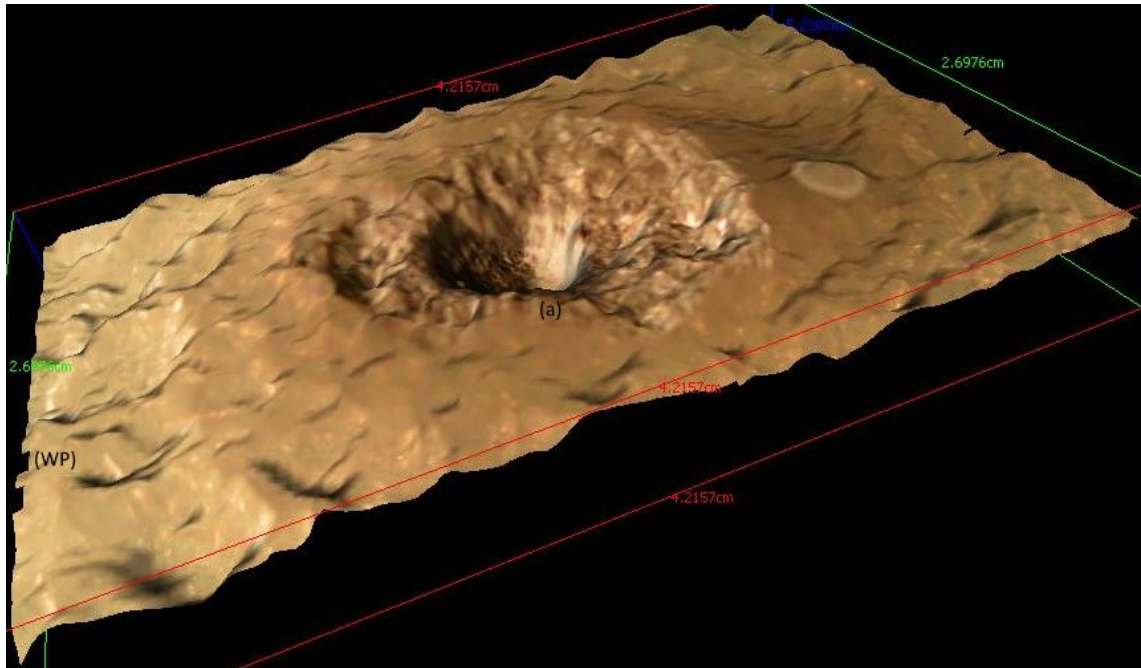


Figure 35 - 3D image of the impact crater formed by the hypervelocity impact on the soda lime glass target at 30°. The (WP) marker shows the witness plate end of the glass block, and (a) shows the central crater pit.

The 3D image in Figure 35 clearly shows the central crater pit formed in the impact, as well as the areas around the pit that were dislodged. Due to the shattered glass surface, the glass surface has a more rippled appearance compared to the aluminium surfaces. The areas of dislodged material around the crater mentioned and seen previously in Figure 31 can be more easily seen here, and a better understanding can be had of the amount of shattering the glass underwent in the impact due to actually seeing the crater pit, the dislodged target material area and more of the target plate all in one image.

3.2.2 45 Degrees – G110216/1

The crater formed for the 45° shot was quite different to that of the 30° shot. This crater did not have as much target material dislodged in the impact, all that could be seen was the crater pit and the shattered glass target block. This can be seen in the following figure.

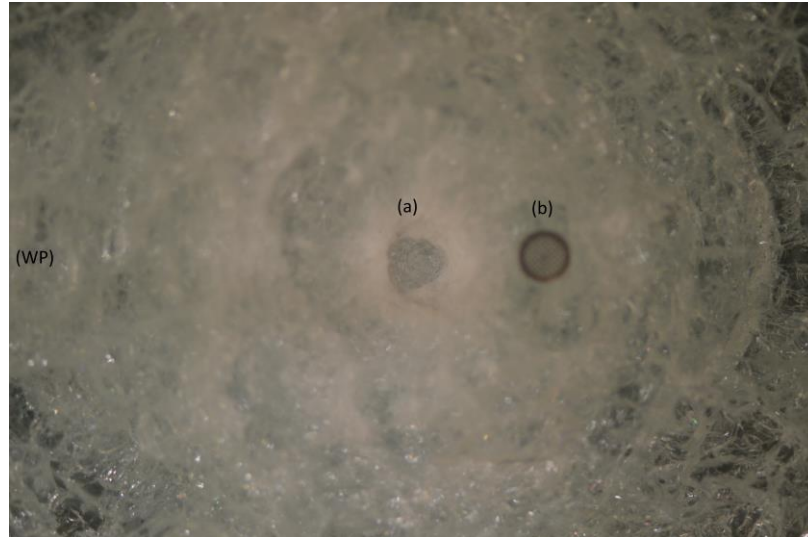


Figure 36 - Image showing the impact crater formed on the soda lime glass target at 45°. The (WP) marker shows the end of the target where the witness plate was fixed, (a) shows the crater pit, and (b) is the 2.5mm size marker.

The projectile came into contact with the glass target 37.5mm from the witness plate, and zirconium was first seen at a height of 23mm within the secondary ejecta pattern. The calculated minimum angle that the projectile matter moved away from the impact would have been 31.522°. The ejecta pattern present on the witness plate was seen to have the now familiar 'V' shaped fan pattern, but it also seemed to have an area of cratering high up in the centre of the fan arms, as well as some pitting and cratering between these two regions, and some trails below the centre of the fan.



Figure 37 - Image of the secondary ejecta pattern. The fan arm can be seen bounded by the curved black line, the black circle shows the high up central area of cratering, the two red circles show the pitting between those two regions, and the white circle shows the area that had some kind of trails present below the fan centre.

Below is a colourised elemental image showing the secondary ejecta pattern on the copper witness plate.

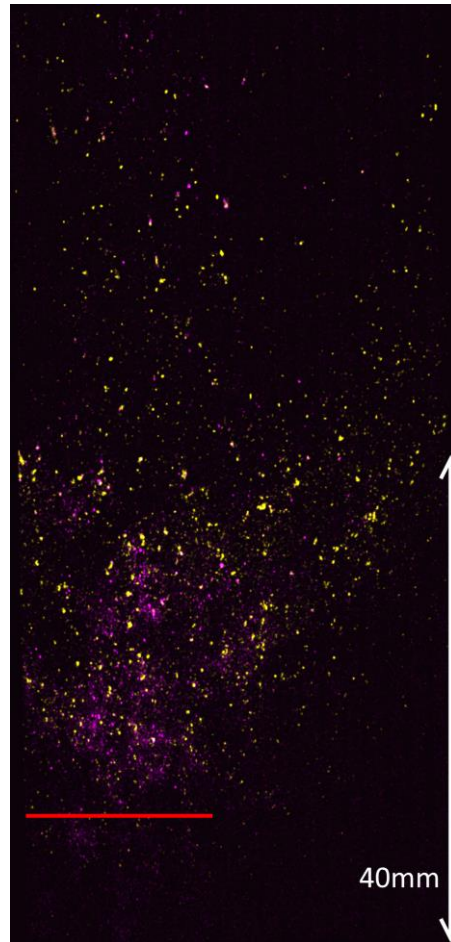


Figure 38 - Colourised elemental image of the secondary eject pattern. Zirconium is seen in pink, and Silicon is seen in yellow. The red line marks the start of the zirconium in the ejecta material, showing where the previous measurement for the height was taken from.

As seen in Figure 38, the familiar 'V' shaped pattern is obviously visible, where the arms of the fan seem to be mainly made up from silicon. The central area of the fan has mixed composition; some larger chunks of silicon are present, with a very high amount of fine dust like zirconium visible. There are only a handful of other areas in the ejecta pattern where zirconium can be seen; one is the high up central region between the fan arms, and another is the centre of the fan arms themselves. The high up central region seems to be dominated by silicon, just like the fan arms, but there is some zirconium present much higher up in this region.

Upon closer analysis of the lower central region near the base of the fan, it was found that a handful of large craters – ranging between 85.9microns to 217microns long – were present and surrounded by many smaller craters and

extremely fine pitting. Some of the smaller craters were seen with sizes between 21.6microns to 52.8microns, but the majority of them were on the smaller side of the scale. The fine pitting seen on the other was even smaller, mostly around 2.27microns across. The craters seem to have both projectile and target plate matter present; the zirconium looks to be in small chunks, usually on the walls of the crater or on the crater lip, whereas the silicon seems to be more dust like but still present in the same areas as zirconium.

When analysing the lower down fan area, craters with a size of around 20microns across dominated the area, with some fine pitting between. Some of the biggest craters seen were around 190microns in length, but there were extremely rare with only a few of this size present in the lower edge of the fan. The fine pitting seen between the small craters were all very similar sizes, mostly all around 3microns across. In this area of the fan, silicon was the element seen most abundantly, present in chunks in some of the slightly larger craters, deposited in the surface of the copper plate in large pieces (some pieces being over 70microns long), and even some seen on the lip of smaller craters. Zirconium was seen within this area of the fan, it was just not as common as the silicon; it was seen within some of the smaller craters of sizes between 8.52 microns and 28.5microns, the lips of some slightly larger craters, and also seen slightly mixed with the large chunks of silicon on top of the plate's surface.

When investigating the higher edge of the fan arm, it was seen that the number, and overall size, of craters had diminished. Most craters were around 10microns across, though a handful of slightly larger and slightly smaller craters were seen. Dotted around the area where some larger gouge-type features, seen to be between 114microns to 175microns long. These gouges seemed to be dominated by either one of the main elements, with very small amounts, if any at all, of the other; the shorter gouges were much higher in zirconium material, whereas the long features contained a much larger amount of silicon.

The high-up central region of the ejecta pattern consisted of many craters, with sizes ranging between 7.04microns to just over 105microns wide, though most seemed to be around 45microns across. Some larger craters – one measured

to be 386microns across – were present in the area, but only very, very rarely were any seen of this size. Once again, fine pitting on the copper surface was present, with the small pits being 2.33microns across at their largest. Looking at the elemental abundancies in this area, and in keeping with what is seen in Figure 41, there was a slight mixing between the zirconium and silicon; the larger craters were dominated by zirconium, but the shallow looking craters were lined with silicon. Zirconium was usually found coating one of the walls of the larger craters, whereas silicon was seen to either line the base of the craters it inhabited, or to flatter crater edge lips.

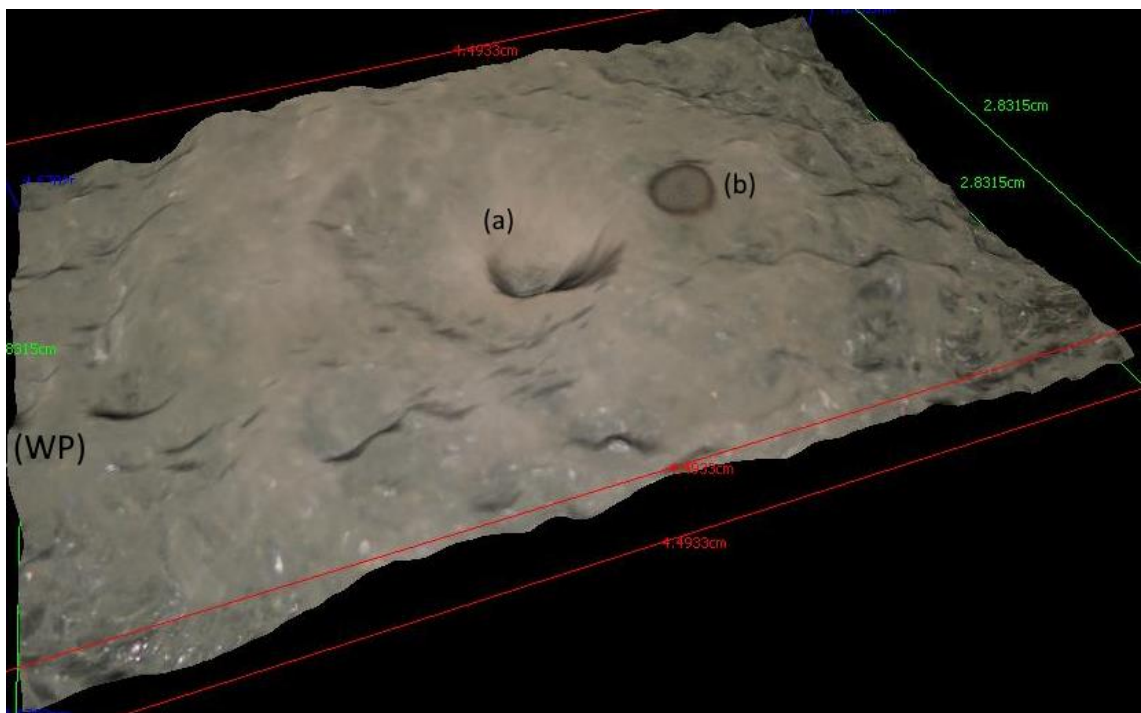


Figure 39 – 3D image of the impact crater in the soda lime glass target. (WP) shows the end of the glass block where the witness plate was fixed, just below (a) is the impact crater pit, and (b) is the 2.5mm size marker.

Due to the surface of the glass target shattering outwards after the hypervelocity impact, the 3D image compiled in Figure 29 does become somewhat distorted; as you look away from the impact crater at (a) towards the edge of the glass block, the surface looks almost rippled. Even with the distortion present, the impact crater is still visible, and the rippling effect on the image helps to understand the state of the glass target post-impact.

3.2.3 60 Degrees – G110316/2

The impact crater for the 60° target set up is again different from the previous two craters in the soda lime glass target blocks. Similar to before, the glass had shattered dramatically due to the impact. But unlike before, the impact dislodged material from only one side of the impact crater.

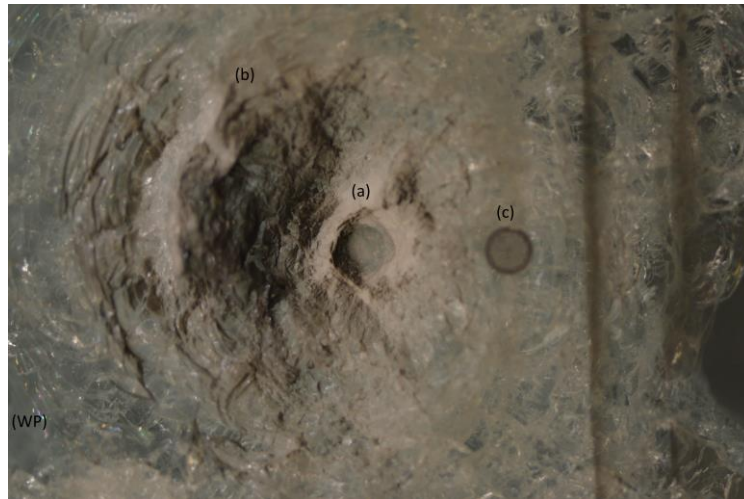


Figure 40 - Image showing the impact crater in the soda lime glass target, where (WP) shows the end of the glass block where the witness plate is fixed, (a) is the crater pit, (b) is the area of dislodged material from the glass block, and (c) is the 2.5mm size marker.

Looking at Figure 40, the crater can be seen directly in the middle of the image (a), with the dislodged glass material to the left of it (b). It can be seen when looked at closely, that the dislodged material came off of the block in almost two distinct places; one being the curved area with the markers (a) and (b) on Figure 40, and the second is the area to the left of the white line just below the (b) marker.

This impact had occurred 56mm away from the witness plate, and projectile material was first seen 15mm up from the base of the witness plate in the secondary ejecta pattern; this means that the projectile material travelled away from the impact site at a minimum angle of 14.995°. The secondary ejecta pattern on the copper witness plate once again had the 'V' fan shape present, and it also consisted of a large area of trailing marks below the centre of fan. In the high-up centre of the V-fan arms, there was a very well defined 'peak' shape

of cratering – similar had been seen in previous shots, but the definition of this ‘peak’ shape was so much more solid in the ejecta pattern.

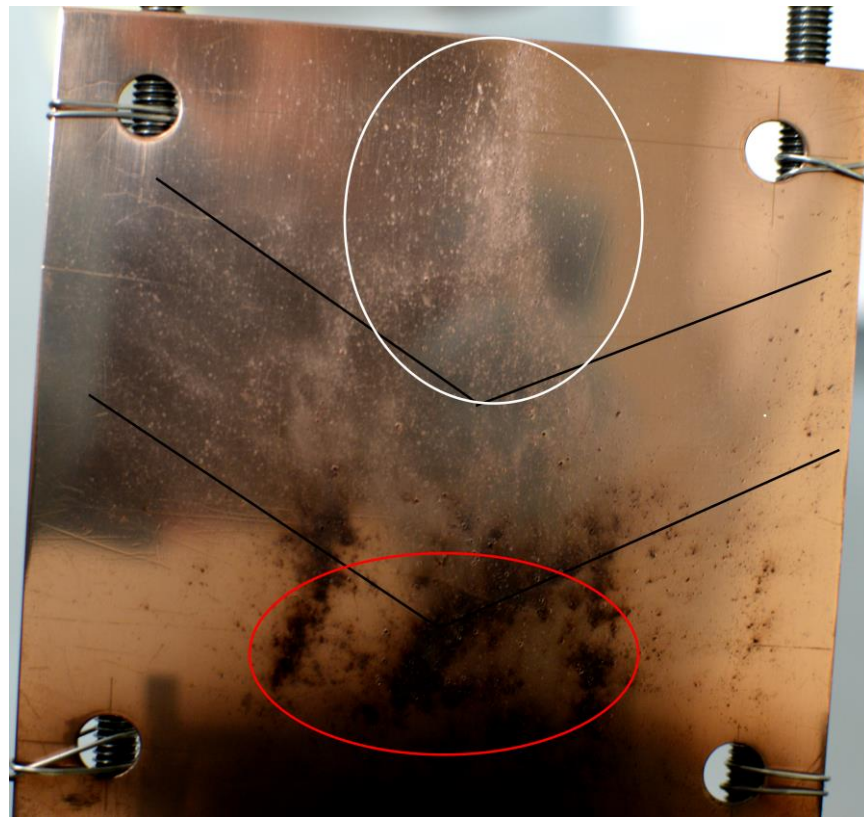


Figure 41 - Image displaying the secondary ejecta pattern on the copper witness plate. The black chevron indicates the previously seen fan pattern, the red ellipse shows the area below the fan centre made up of trailing marks, and the white ellipse bounds the now better-defined ‘peak’ pattern.

Both ‘peak’ shape and trail marks shown in Figure 41 had been seen in the previous soda lime glass target shots, but neither of the features had been as well defined or visibly obvious as they were here.

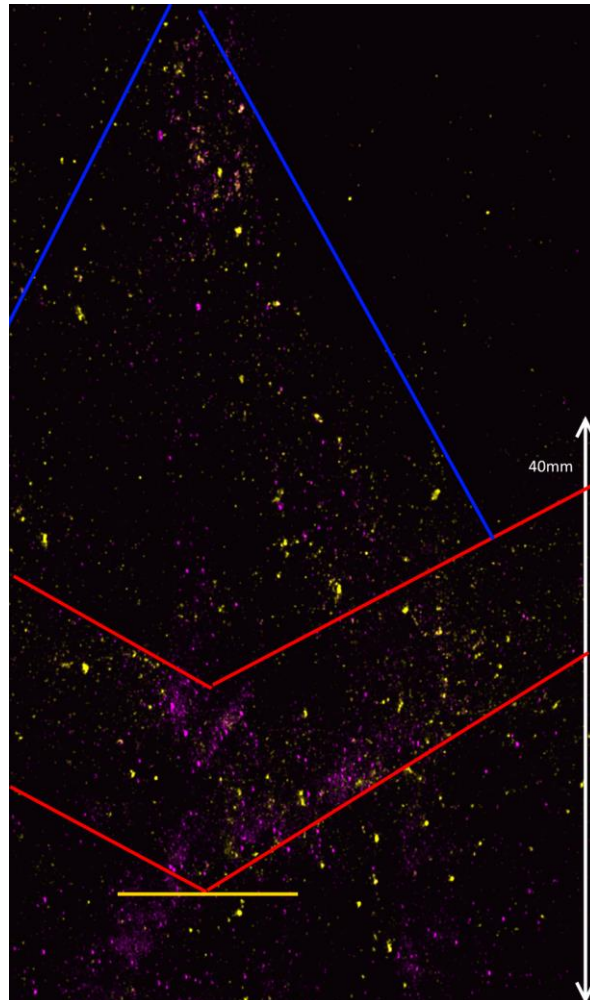


Figure 42 - Colourised elemental image of the secondary ejecta pattern. Pink was used for the zirconium, whilst yellow was used for silicon. The horizontal yellow line demonstrates where the projectile material within the fan began (where the height measurement was made to for Figure 12), the red chevron illustrates the arms of the fan pattern, and the blue lines bound the now newly seen 'peak' shape from Figure 44.

As it can be seen in Figure 42, there is considerable amount more fine dust like zirconium present within the ejecta pattern than silicon. Much of it is found at the centre of the fan pattern, but some can also be seen within the trail marks below the fan, and on the outside edge & central line of the 'peak' pattern higher up on the plate. The silicon is seen mostly in more defined chunks than the zirconium, where these chunks seem to follow the arm of the fan, the edge of the peak pattern, and the trail marks below the fan.

When analysing a section from the centre area of the fan, many different sized craters were found, along with some fine pitting; the majority were less than

43.8microns across, but some as long as 184microns and bigger were seen. The fine pitting marks were 1.73microns to 3.51microns across. The zirconium material was seen to be present with the craters that measured upwards of 60microns across, but also seen in some smaller craters that were shallower in appearance. The silicon was found to be present in the smaller craters as both a fine dust and as small chunks measuring up to 17microns long.

When a section of the fan arm was analysed, it was seen that, again, many craters were found, but this time the majority of them were all around 100microns in length; there were a handful of craters that were bigger than these, but the ~100micron-sized craters dominated population-wise. Similar to the fan-centre analysis, zirconium was usually found within larger craters with a size range of 42microns to 130microns across, and silicon matter was found either in the very small craters of size 16-24microns, or as small chunks within larger craters which also housed some projectile matter. When looking at the images for the analysis of this area, it was quite difficult to see the fan-arm pattern which had previously been seen in other analysis images on other witness plates; the craters were far too high number and too close together to view the same pattern as seen before.

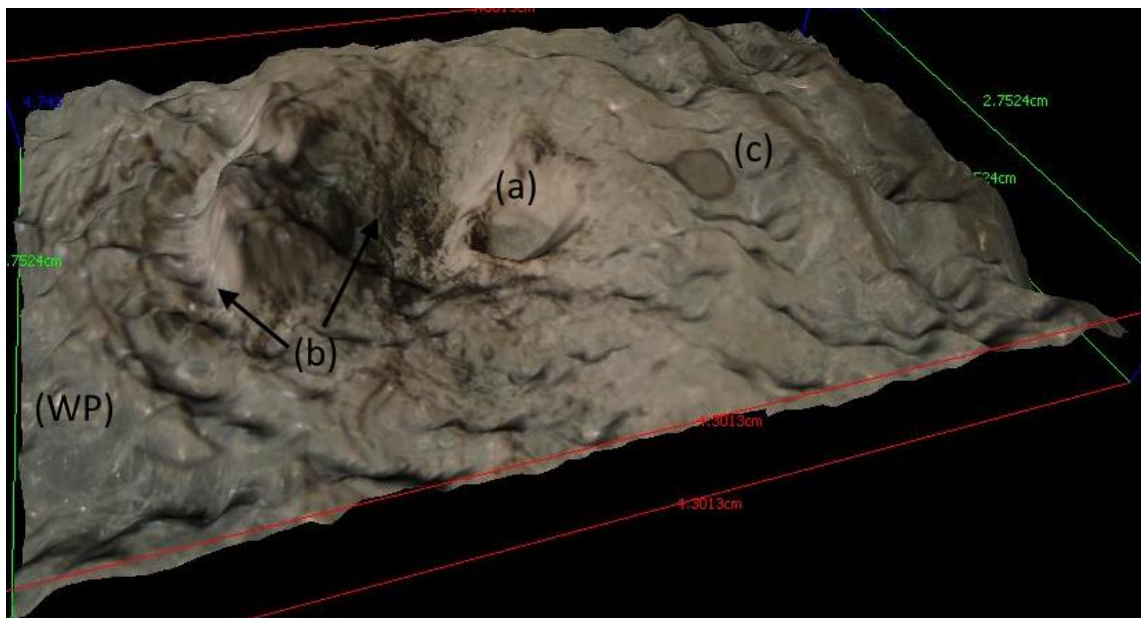


Figure 43 - 3D image of the impact crater seen in Figure 43, where (WP) is the end of the block where the witness plate was fixed, (a) is the impact crater, (b) shows the two areas of target material dislodged in the impact, and (c), the 2.5mm size marker.

Once again, due to the shattered surface of the soda lime glass target block, the 3D image in Figure 43 appears somewhat more distorted than it actually. The peak between the two dislodged material troughs at marker (b) is a lot more pronounced than it is on the actual block, but it gives an idea of the two separate areas that were dislodged in the impact.

Chapter Four: Results from the Hydrocode Modelling Simulations

4.1 Aluminium Targets

This section will display the results found using the hydrocode modelling simulations for the aluminium targets at the three experimental angles. This section will mainly be images from the models run, and a discussion of what can be seen within the images.

4.1.1 30 Degrees

The following figure shows the end of the hydrocode model run, including the aluminium target block and the secondary ejecta captured on the subroutine 'witness plate'.

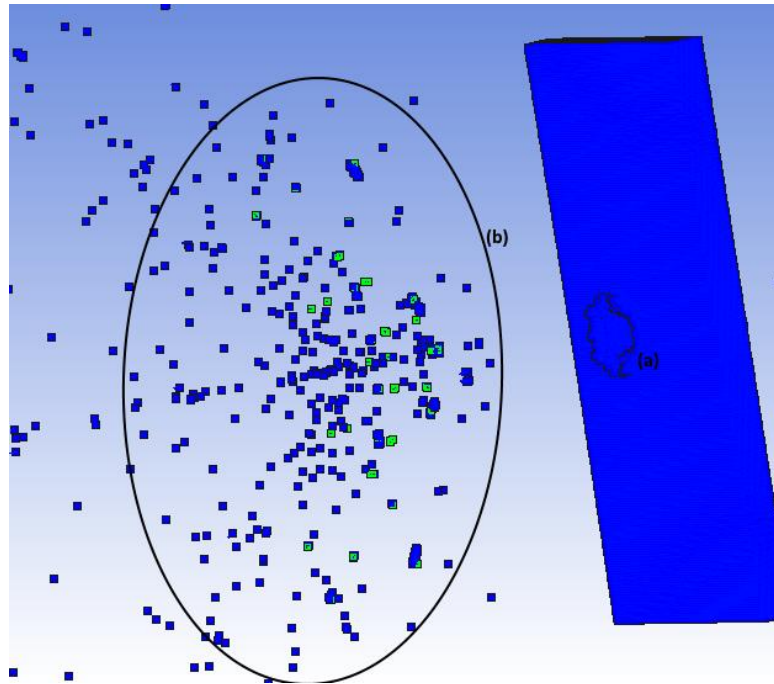


Figure 44 - Screenshot showing the final slide of the hydrocode modelling simulation, where the aluminium material is in blue, the zirconium is in green, the target plate and impact crater are shown by (a), and the secondary ejecta pattern is within the ellipse (b).

The now well known 'V' fan formation can be seen within the secondary ejecta pattern inside the ellipse in Figure 44. The main component of the ejecta pattern is modelled to be aluminium (the small blue squares), and only a small amount of the pattern is made up for zirconium from the projectile (the small green squares). The projectile matter is seen to only be present lower down within the fan, whereas the aluminium can be seen to be present at all points of the ejecta pattern.

4.1.2 45 Degrees

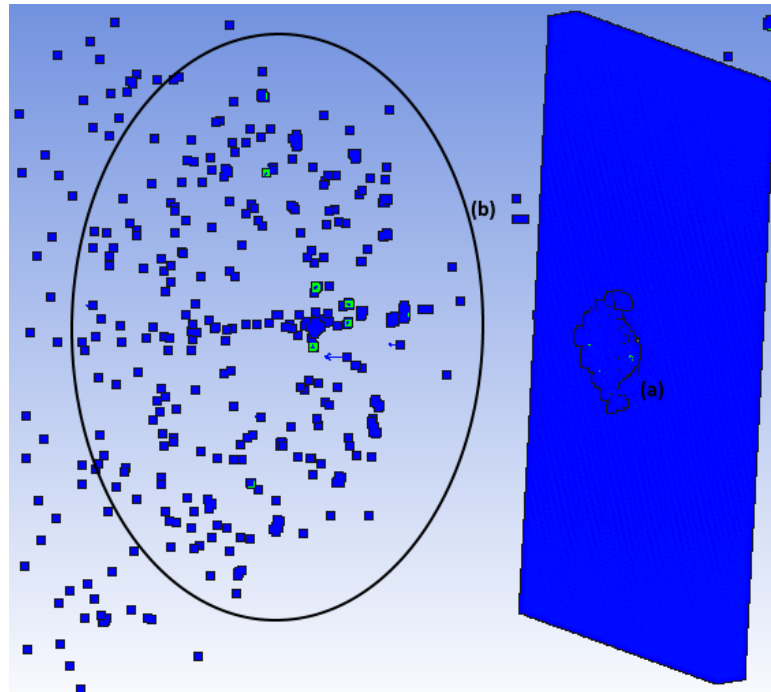


Figure 45 - Screenshot of the hydrocode modelling simulation showing the aluminium target plate and crater at (a) and the secondary ejecta pattern inside of the ellipse (b). Aluminium is coloured blue, and zirconium is coloured green.

Looking at Figure 45, there is a lot less zirconium present within the secondary ejecta pattern than aluminium, and the 'V' shaped pattern of the ejecta is not that visible. The pattern displayed within the simulation seems to be that of a number 8 instead of the distinct fan arms seen. Looking lower down at the pattern (closer to the aluminium target block), the fan arms can be made out, but as they move away from the target block, they start to curve back towards the centre of the pattern, giving it the number 8 appearance.

4.1.3 60 Degrees

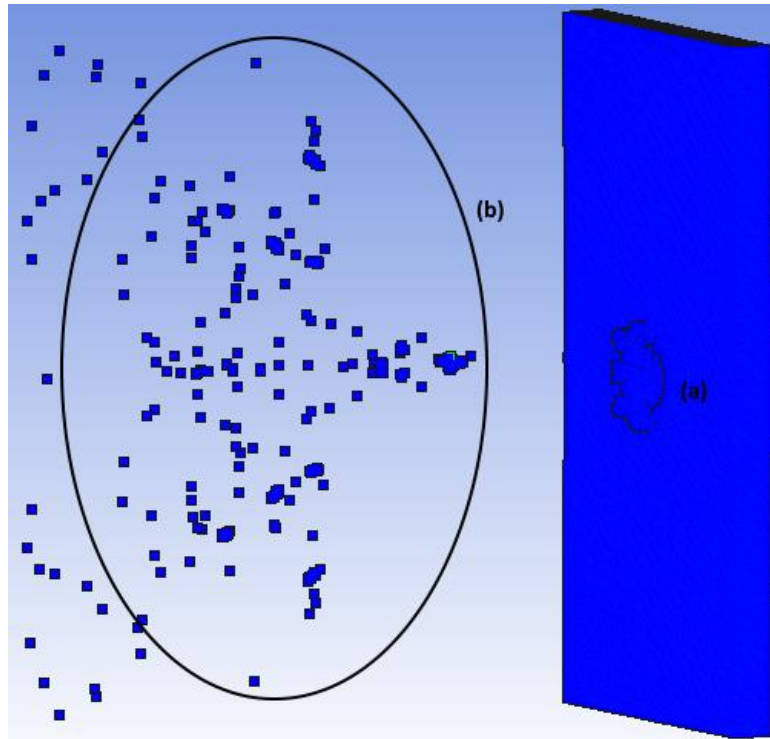


Figure 46 - Image of the hydrocode modelling simulation end point displaying the aluminium target block and crater at (a) and the secondary ejecta pattern within the ellipse (b). Aluminium is coloured blue and zirconium is coloured green.

The secondary ejecta pattern seen in Figure 46 is again different to those seen previously. The pattern is less of a 'V' shaped fan with arms, and more of a filled in letter 'V'. There are no distinct arms seen within the pattern, but still holds true to the 'V' outline. Regarding the elemental make up for the ejecta in the simulation, there is next to no zirconium present, only a very small amount extremely low down in the ejecta pattern; near enough the whole ejecta pattern is made up from aluminium.

4.2 Soda Lime Glass Targets

This section will display results obtained from the hydrocode modelling simulations using the soda lime glass target set-up. Only one angle, 45° , was successfully modelling using Autodyn; this was due to the complexity of the model creation prior to running the model simulation. As the simulation needed to be as close to the real experimental shots as possible, the glass block

thickness had to be replicated (the soda lime glass block dimensions were 114x62x18mm). As the simulation used the SPH part filler in Autodyn, so as to gain the most in-depth results possible, it created a massive amount of moving particles for the simulation to calculate. This huge number of particles dramatically increased the calculation time for each step the simulation took, meaning the simulation ran for an extremely long time to gain just the results for the one angle that will be presented here.

4.2.1 45 Degrees

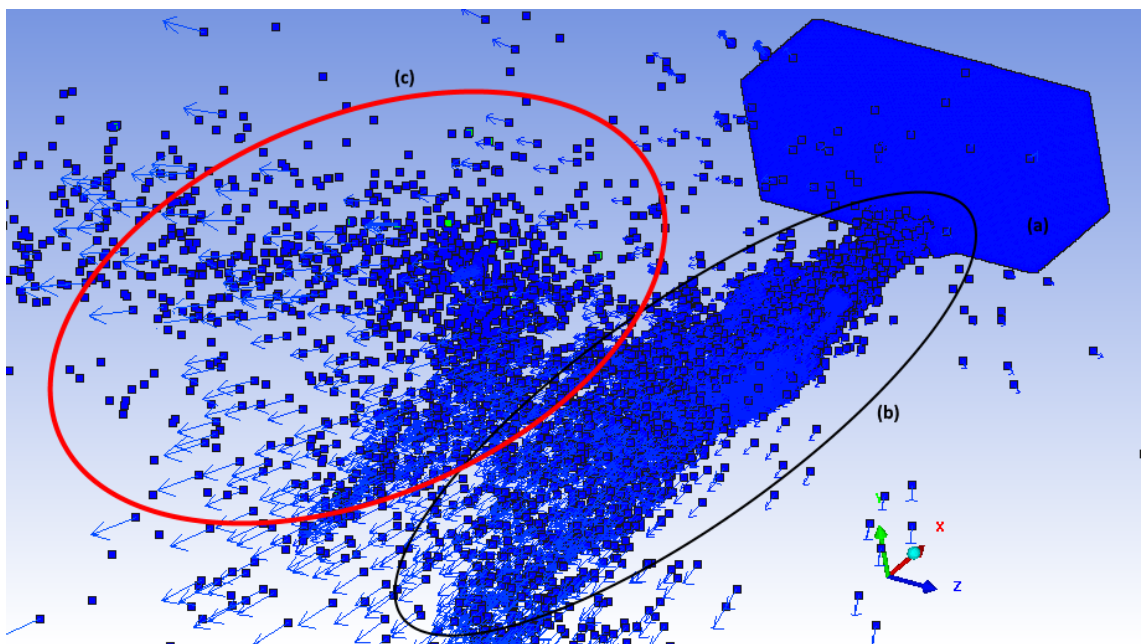


Figure 47 - Image showing the end point of the hydrocode simulation for the soda lime glass target set up at 45°. The blue block marked (a) is the soda lime glass target, the black ellipse (b) is material that was simulated to have been blasted outwards from the impact crater, and the red ellipse (c) shows the secondary ejecta. The soda lime glass is coloured blue in this simulation, with the zirconium coloured green.

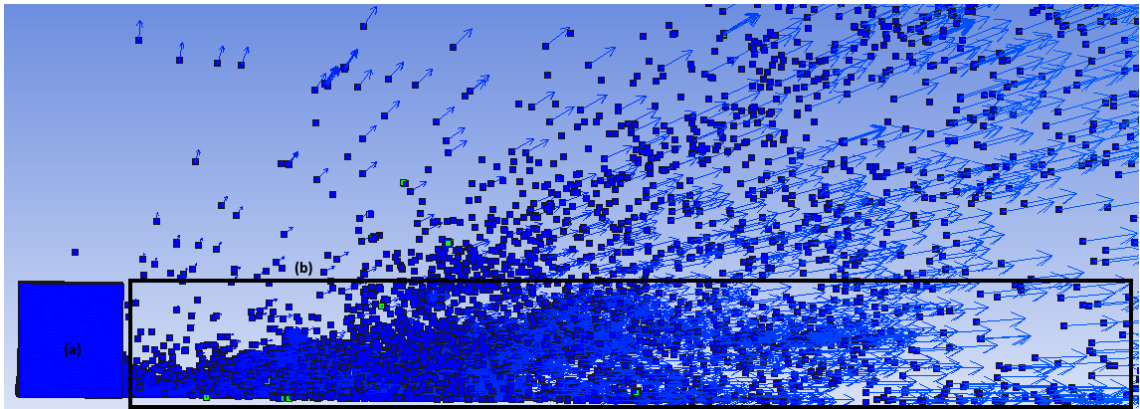


Figure 48 - Image from the hydrocode modelling simulation for the 45° soda lime glass target set up. This image shows the same information, from the same time step, as Figure 50, just from a different perspective. The glass target is shown by (a), and the ejecta pattern, seen here as front on, is partially contained within the rectangle (b).

As previously explained, and evident in Figures 47 & 48, the set-up of the soda lime glass target created an extremely high number of moving particles. Due to this, it is quite difficult to see ejecta pattern in Figure 47. In Figure 47, it can be seen that, not only did the simulation predict secondary ejecta to deposit on the witness plate, but it also predicted a massive amount of matter to be ejected directly out of the impact crater; this extra ejected matter obscured the secondary ejecta, so Figure 48 is displayed to give some idea of the secondary ejecta produced. Looking at Figure 48, it is still very difficult to ascertain what is secondary ejecta and what is not, but the general idea of the 'V' shaped fan can be seen by looking at the matter moving away from the rectangle (b). The arrows associated with each particle are there to display its speed and movement direction; looking at these vectors, the familiar 'V' pattern can be assumed as present within the simulation, but do have to be taken with a pinch of salt, as the particle seen maybe those ejected from the impact crater.

Chapter Five: Conclusions

Looking back over the results found for both the hypervelocity impact experiments and the hydrocode modelling, some similarities are evident and seen within what has been present here, and some stark differences have been found.

Just within the laboratory impact experiment type, the main similarity found was that to do with the secondary ejecta pattern. Across all of the experimental shots, using the two different target types and the three different angles, the ejecta pattern almost always form the 'V' shaped fan. The same shape, including the fan like structure and distinct 'V' like arms, could be seen in nearly all ejecta photos and elemental image maps – more obviously so in the elemental image maps as it was more apparent where the projectile and target material ended up on the witness plates with seeing extra craters, gouges, splats, or other material that could otherwise obscure the pattern from view. The measured information, such as the angle of projectile matter leaving the impact crater and the spread of projectile matter within the ejecta patterns also followed the same trend between angles of the same target type; the projectile matter's angle leaving the impact site always decreased as the angle of impact for the projectile onto the target plate increased (measurements can be seen in Figure 12), and the spread of projectile and target matter contained within the ejecta patterns also moved in the same fashion between differing angles. But this is where main similarities end.

When compared to the results found using the hydrocode modelling software, the same type of ejecta pattern was present (for the aluminium targets at the very least), but the physical spread of projectile matter within the pattern was drastically different, and much less abundant. It is unknown why this is, but it is assumed that the modelling software would need more in-depth user parameters set for the material types and particle erosion type to correctly simulate the light gas gun experimental shots. When comparing the 45° soda lime glass experimental shot results with the Autodyn simulation, the only

definite similarity that can be seen is that the impact will create a secondary ejecta pattern, with a very loosely similar 'V' shaped appearance; due to the extreme complexity of the set-up and results, and the extra information seen by where matter is ejected straight out of the impact crater, it is very difficult to see any other similarities or differences, apart from the lack of projectile matter within the secondary ejecta pattern.

For more meaningful results in future endeavours, it would be ideal to complete more experimental shots using the light gas gun, this time looking at other angles than just the three chosen for these experiments, and also possibly utilising different target and projectile materials. In terms of the hydrocode modelling, many more simulations would need to be run, either setting them up in a simpler fashion, or to input more user chosen parameters and to allow the simulations to run for longer (hoping for no more errors along the way forcing the simulation to end prematurely) to give more meaning, and hopefully, more accurate representations of the laboratory experiments.

In terms of the main aim for this thesis, it is inconclusive whether our knowledge of hypervelocity impacts in low Earth orbit is sufficient enough to create the most up to date and ideal protection systems for satellites and spacecraft that could inhabit this area of space. That being said though, in terms of replicating the laboratory experiments using hydrocode modelling simulations, it is clear from the results found here that work still needs to be done for hydrocode models to correctly and accurately simulate real life impacts of the kind carried out during this research.

References

Journals and Proceedings

Bernhard R. P., Christiansen E. L. and Kerr J. H. 2001. Space Shuttle Meteoroid and Orbital Debris Impact Damage, *International Journal of Impact Engineering*, 26:p33-38

Bernhard R. P., Christiansen E. L. and Kessler D. E. 1997. Orbital debris as detected on exposed spacecraft, *International Journal of Impact Engineering*, 20:p111-120

Bradley A. M. and Wein L. M. 2009. Space debris: Assessing risk and responsibility, *Advances in Space Research*, 43:p1372-1390

Burchell M. J., Cole M. J., McDonnell J. A. M. and Zarnecki J. C. 1999. Hypervelocity impact studies using the 2MV Van De Graaff accelerator and two-stage light gas gun of the University of Kent at Canterbury, *Measurement Science & Technology*, 10 (1):p41-50

Carpenter J. D., Stevenson T. G., Fraser G. W., Lapington J. S. and Brandt D. 2005. Dust detection in the ISS environment using filmed microchannel plates, *Journal of Geophysical Research*, Vol. 110, E05013

Christiansen E.L., Hyde J. L. and Bernhard R. P. 2004. Space Shuttle Debris and Meteoroid Impacts, *Advances in Space Research*, 34:p1097-1103

Collins G. S. 2002. *An Introduction to Hydrocode Modelling*, Applied Modelling and Computation Group, Imperial College London

Collins G. S., Melosh H. J., and Ivanov B. A. 2004. Modelling damage and deformation in impact simulations, *Meteoritics & Planetary Science*, 39(2):p217-231

Davidson T. M., Collins G. S., Elbeshhausen D., Wünnemann K. and Kearsley A. 2011. Numerical modelling of oblique hypervelocity impacts on strong ductile targets, *Meteoritics & Planetary Science*, 46(10):p1510-1524

Giannuzzi L. A., Drown J. L., Brown S. R., Irwin R. B. and Stevie F. A. 1997. Focused Ion Beam Milling and Micromanipulation Lift-Out for Site-Specific Cross-Section TEM Specimen Preparation, *MRS Proceedings*, Cambridge University Press, 480:p19

Graham G. A., Kearsley A. T., Butterworth A. L., Bland P. A., Burchell M. J., McPhail D. S., Chater R., Grady M. M. and Wright I. P. 2004. Extraction and microanalysis of cosmic dust captured during sample return missions: laboratory simulations, *Advances in Space Research*, 34:p2292-2298

Graham G. A., Kearsley A. T., Grady M. M., Wright I. P., Griffiths A. D. and McDonnell J. A. M. 1999. Hypervelocity Impacts in Low Earth Orbit: Cosmic Dust Versus Space Debris, *Advances in Space Research*, 23(1):p95-100

Graham G. A., Kearsley A. T., Wright I. P., Grady M. M., Drolshagen G., McBride N., Green S. F., Burchell M. J., Yano H. and Elliot R. 2001. Analysis of Impact Residues on Spacecraft: Possibilities and Problems, In: *Proceedings of the Third European Conference on Space Debris*, ESA Publications Division, p197-202

Heaney P. J., Vicenzi E. P., Giannuzzi L. A. and Livi K. J.T. 2001. Focused ion beam milling: A method of site-specific extraction for microanalysis of Earth and planetary materials, *American Mineralogist*, 86(9):p1094-1099

Hörz F., Zolensky M. E., Bernhard R. P., See T. H. and Warren J. L. 2000. Impact Features and Projectile Residue in Aerogel Exposed on Mir, *Icarus*, 147(2):p559-579

Johnson N. L., Krisko P. H., Liou J. -C. and Anz-Meador P. D. 2001. NASA's new breakup model of EVOLVE 4.0, *Advances in Space Research*, 28(9):p1377-1384

Johnson N. L., Stansbery E., Liou J. –C., Hortsman M., Stokely C. and Whitlock D. 2008. The characteristics and consequences of the break-up of the Fengyun-1C spacecraft, *Acta Astronautica*, 63(1-4):p128-135

Kearsley A. T., Drolshagen G., McDonnell J. A. M., Mandeville J. –C., and Moussi A. 2005. Impacts on Hubble Space Telescope solar arrays: Discrimination between natural and man-made particles, *Advances in Space Research*, 35:p1254-1262

Kessler D. J. and Cour-Palais B. G. 1978. Collision frequency of artificial satellites: The creation of a debris belt, *Journal of Geophysical Research: Space Physics*, 83(A6):p2637-2646

Liou J. –C., Hall D. T., Krisko P. H. and Opiela J. N. 2004. LEGEND – a three-dimensional LEO-to-GEO debris evolutionary model, *Advances in Space Research*, 34:p981-986

See T., Allbrooks M., Atkinson D., Simon C. and Zolensky M. 1990. Meteoroid and Debris Impact Features Documented on the Long Duration Exposure Facility, Space & Life Sciences Directorate, Solar System Exploration Division, Planetary Science Branch, Publication #84, JSC #24608

Wang T. 2010. Analysis of debris from the collision of the Cosmos 2251 and the Iridium 33 satellites, *Science & Global Security*, 18(2):p87-118

Warren J. L., Zook H. A., Allton J. H., Clanton U. S., Dardano C. B., Holder J. A., Marlow R. R., Schultz R. A., Watts I. A. and Wentworth S. J. 1989. The Detection and Observation of Meteoroid and Space Debris Impact Features on the Solar Max Satellite, In: *Proceedings of the 19th Lunar and Planetary Science Conference*, Lunar and Planetary Science Institute, Houston, p641-657

Westphal A. J., Snead C., Borg J., Quirico E., Raynal P. I., Zolensky M. E., Ferrini G., Colangeli L. and Palumbo P. 2002. Small hypervelocity particles captured in aerogel collectors: Location, extraction, handling and storage, *Meteoritics & Planetary Science*, 37:p855-865

Wirth R. 2009. Focused Ion Beam (FIB) combined with SEM and TEM: Advanced analytical tools for studies of chemical composition, microstructure and crystal structure in geomaterials on a nanometre scale, *Chemical Geology*, 261(3-4):p217-229

Wozniakiewicz P. J., Kearsley A. T., Burchell M. J., Foster N. J., Cole M. J., Bland P. A. and Russell S. S. 2009. In situ analysis of residues resulting from laboratory impacts into aluminium 1100 foil: Implications for Stardust crater analyses, *Meteoritics and Planetary Science* 44(10):p1541-1559

Zolensky M. E., See T. H., Bernhard R. P., Barrett R., Hörz F., Warren J. L., Dardano C., Leago K. S., Kessler D. and Foster T. R. 1995. Final Activities and results of the Long Duration Exposure Facility, Meteoroid and Debris Special Investigation Group, *Advances in Space Research*, 16(11):p53-65

Websites

Alicona n.d., That's Metrology!, <http://www.alicon.com/produkte/mex/> (Accessed 25th February 2018)

NASA n.d., Orbital Debris Radar Measurements, <http://orbitaldebris.jsc.nasa.gov/Measurements/radar.html> (Accessed 25th February 2018)

Union of Concerned Scientists 2017, UCS Satellite Database, <http://www.ucsusa.org/nuclear-weapons/space-weapons/satellite-database#.VwLkn6QrLIU> (Accessed 25th February 2018)